An ESCRT grommet cooperates with a diffusion barrier to maintain nuclear integrity

Nicholas R. Ader, Linda Chen, Ivan V. Surovtsev, William L. Chadwick, Megan C. King*, and C. Patrick Lusk*

Department of Cell Biology, Yale School of Medicine, 295 Congress Ave, New Haven, CT, 06520

* Correspondence: patrick.lusk@yale.edu, megan.king@yale.edu

ABSTRACT

The reformation of the nuclear envelope (NE) at the end of metazoan mitosis requires the sealing of numerous fenestrations that recruit the endosomal sorting complexes required for transport (ESCRT) machinery. The molecular mechanisms by which ESCRT proteins drive NE sealing and their necessity to the reestablishment of the nuclear compartment have yet to be fully defined. Here, we leveraged the single NE hole generated by mitotic extrusion of the *Schizosaccharomyces pombe* spindle pole body to reveal two modes of ESCRT function carried out by unique complements of ESCRT-III proteins, both of which depend on the NE-specific CHMP7/Cmp7. The first is a grommet-like function, where we tie the presence of specific ESCRTs to a constriction of the NE hole from ~150 to ~50 nm in anaphase B. Consistent with a direct role for ESCRTs in restricting this NE hole diameter, the hole dilates a remarkable five-fold in cells lacking Cmp7. Second, in the subsequent G_1/S-phases, a sealing module of ESCRT proteins replaces Cmp7 and is required to drive closure of the NE. Surprisingly, in the absence of Cmp7, nucleocytoplasmic compartmentalization remains intact despite discontinuities in the NE as large as 400 nm, suggesting a mechanism to establish a diffusion barrier(s) over persistent NE holes. Indeed, we demonstrate that the ortholog of the pericentriolar material protein, pericentrin (Pcp1), establishes such a barrier, likely through its ability to form a biomolecular condensate. NE remodeling mechanisms therefore cooperate with proteinaceous diffusion barriers beyond nuclear pore complexes to protect the nuclear compartment.

36 **INTRODUCTION**

37 In eukaryotic cells, the genome is enclosed by the nuclear envelope (NE), which
38 contributes to the establishment of a protected nuclear compartment. The NE is
39 contiguous with the endoplasmic reticulum (ER) but is functionally specialized due to a
40 unique proteome that populates its constituent inner, outer, and nuclear pore membranes.
41 Nucleocytoplasmic compartmentalization relies on the integrity of these membranes and
42 the selective barrier properties of nuclear pore complexes (NPCs) embedded in the NE
43 (Dultz et al., 2022). During mitosis, the NE barrier presents a challenge for the spindle as
44 it must access the duplicated chromosomes to faithfully segregate the genome to each
45 daughter cell. Evolution has provided several solutions to this problem with a continuum
46 of "closed" to "open" mitosis mechanisms employed in different organisms that reflects
47 the degree to which the NE remains globally intact during chromosome segregation
48 (Makarova and Oliferenko, 2016). Regardless, elaborate changes to the morphology of
49 the NE during this period are universally observed, helping to ensure either the
50 maintenance (in the case of a closed mitosis) or re-establishment (in the case of an open
51 mitosis) of nucleocytoplasmic compartmentalization (Ungricht and Kutay, 2017).

52 These NE remodeling mechanisms are perhaps most elaborate at the end of the
53 open mitosis of mammalian cells, when decondensing chromosomes are surrounded by
54 nascent NE. Completion of NE sealing requires the closing of numerous NE fenestrations
55 through an annular fusion mechanism thought to be executed by the endosomal sorting
56 complexes required for transport (ESCRT) machinery, specifically the ESCRT-III proteins
57 (Gu et al., 2017; Olmos et al., 2015; Olmos et al., 2016; Ventimiglia et al., 2018; Vietri et
58 al., 2015; von Appen et al., 2020). A similar mechanism has been invoked in the sealing
59 of nuclear pores housing defective NPCs (Thaller et al., 2019; Thaller et al., 2021;
60 Webster et al., 2014; Webster et al., 2016) and at NE ruptures frequently observed in
61 cancer cells (Denais et al., 2016; Raab et al., 2016). While the events that underlie
62 ESCRT-III mediated NE sealing have not been mechanistically delineated, parallels have
63 been drawn with more extensively studied ESCRT-mediated membrane fission reactions.
64 For example, during intralumenal vesicle (ILV) formation on endosomes, ESCRT-I/II
65 recruit and activate the polymerization of ESCRT-III proteins (Vietri et al., 2020). ESCRT-
66 III proteins can form single- and double-stranded homo and heteropolymer filaments *in*

67 *vitro*; such filaments have affinity for negative or positive membrane curvature, perhaps
68 influenced by the specific ESCRT-III subunit composition (McCullough et al., 2018;
69 Pfitzner et al., 2021; Remec Pavlin and Hurley, 2020). The AAA+ ATPase VPS4 is
70 thought to be critical for the dynamic exchange of filament subunits with a monomer pool
71 (Adell et al., 2017; Mierzwa et al., 2017) and for the ultimate membrane fission step
72 (McCullough et al., 2018).

73 Despite the topological similarity between a NE hole and the neck of forming ILVs,
74 prior studies reveal distinct ESCRT requirements at the NE that hint at potentially unique
75 membrane remodeling and fission mechanisms. For example, ESCRT-I/II are
76 dispensable for the recruitment of ESCRT-III to the NE (Webster et al., 2014). Further,
77 there is an ESCRT-II/III fusion protein, CHMP7 (Chm7 in *Saccharomyces cerevisiae* and
78 Cmp7 in *Schizosaccharomyces pombe/Schizosaccharomyces japonicus*), with a unique
79 function at the NE. Interestingly, unlike most ESCRT-mediated membrane remodeling
80 events that rely on peripheral membrane proteins, the recruitment of CHMP7 to the NE
81 requires a direct physical interaction with an integral inner nuclear membrane protein,
82 LEM2 (Heh1/Src1 in *S.c.* and Heh1/Lem2 in *S.p./S.j.*) (Gu et al., 2017; Webster et al.,
83 2016). *In vitro* (von Appen et al., 2020) and *in vivo* (Thaller et al., 2019) evidence further
84 supports that LEM2 family members also activate CHMP7 polymerization. Additional
85 observations further hint that LEM2 and CHMP7 may form a membrane-embedded co-
86 polymer that lines NE holes like an O-ring, surrounding microtubules that remain attached
87 to kinetochores (von Appen et al., 2020). Lastly, although ESCRT-III subunits including
88 CHMP1A,B (Did2 in yeasts), CHMP2A,B (Vps2 in *S.c.* and Did4 in *S.p./S.j.*), CHMP3
89 (Vps24 in yeasts), CHMP4A,B (Snf7 in *S.c.* and Vps32 in *S.p/S.j.*), and IST1 (Ist1 in
90 yeasts) have been shown to be recruited to the NE alongside additional regulatory factors
91 in metazoans including CC2D1B (Ventimiglia et al., 2018), Nesprin-2G (Wallis et al.,
92 2021) and UFD1 (Olmos et al., 2015), we lack a quantitative spatiotemporal framework
93 including the order, co-dependency, and copy number of ESCRT proteins at a NE sealing
94 site. This information is critical to be able to fully elucidate how (and indeed whether)
95 ESCRTs seal the NE and will also lay the groundwork for further delineation of shared
96 and unique mechanisms that ESCRT proteins engage in to support a diverse range of
97 membrane remodeling activities.

98 Despite clear evidence for recruitment of ESCRT proteins to the NE in late mitosis
99 (Gu et al., 2017; Olmos et al., 2015; Olmos et al., 2016; Ventimiglia et al., 2018; Vietri et
100 al., 2015; von Appen et al., 2020), several observations call into question whether the
101 ESCRT proteins are indeed necessary and/or sufficient to seal the NE. First,
102 compromising ESCRT by depletion of various subunits only delays, but does not
103 abrogate, the re-establishment of the accumulation of a soluble nuclear import reporter
104 into the nucleus after mitotic exit in human cells (Olmos et al., 2015; Olmos et al., 2016;
105 von Appen et al., 2020) and the semi-open mitosis of *S. japonicus* (Lee et al., 2020; Pieper
106 et al., 2020). This result, which was mirrored by orthogonal studies modeling the repair of
107 interphase nuclear ruptures induced by laser ablation (Halfmann et al., 2019) or migration
108 through constrictions (Denais et al., 2016; Raab et al., 2016), suggest that there are
109 alternative, ESCRT-independent mechanisms by which nuclear compartmentalization is
110 reestablished. Indeed, Chm7/Cmp7 is dispensable for cell viability and global
111 nucleocytoplasmic compartmentalization in *S. cerevisiae* (Webster et al., 2016) and *S.*
112 *pombe* (Dey et al., 2020; Gu et al., 2017). One attractive explanation for these
113 observations is the existence of a redundant, ESCRT-independent NE sealing
114 mechanism(s). Indeed, genetic evidence in *Caenorhabditis elegans* and *S. japonicus*
115 suggests that altering phospholipid biosynthesis and/or membrane fluidity can mitigate
116 the ill effects of a compromised ESCRT-dependent NE sealing pathway (Lee et al., 2020;
117 Penfield et al., 2020). Compensation by an orthogonal and CHMP7/Cmp7-independent
118 ESCRT-III sealing mechanism has also been proposed (Lee et al., 2020). It is worth
119 considering, however, that most of these prior studies have relied on an indirect tool to
120 assess the integrity of the NE, namely the nuclear accumulation of a soluble reporter
121 containing a nuclear localization signal (NLS). Direct visualization of the continuity of the
122 NE membranes themselves, although more challenging, is ultimately essential to address
123 whether ESCRTs are necessary for NE sealing.
124 Here, we determine mechanisms of ESCRT function at the NE by taking
125 advantage of the fission yeast *S. pombe*. *S. pombe* inserts and extrudes its spindle pole
126 body (SPB) into and out of the NE at every mitotic entry and exit, respectively (Ding et
127 al., 1997). SPB extrusion thus leaves a single NE hole that must be sealed in each
128 daughter cell in a temporal and topological context similar, but much better defined than,

129 the numerous NE fenestrations present at the final stages of metazoan NE reformation.
130 We performed a comprehensive analysis of the complement, copy number, and relative
131 timing of ESCRT recruitment to the SPB extrusion site correlated to an ultrastructural
132 timeline of NE hole dynamics. In addition to providing definitive data that ESCRTs are
133 essential for ultimately sealing the NE, we also reveal an unexpected role for ESCRTs in
134 restricting the size of the NE hole during anaphase B in a manner akin to the function of
135 a grommet. Last, we uncover a mechanism that can explain the paradox of an apparently
136 intact nuclear compartment containing persistent NE holes: the existence of a
137 compensatory proteinaceous diffusion barrier, one component of which is
138 pericentrin/Pcp1. Our findings thus support both sealing dependent and independent
139 functions for NE-recruited ESCRTs while providing evidence for additional diffusion
140 barriers beyond NPCs that support the integrity of nucleocytoplasmic
141 compartmentalization.
142

143 **RESULTS**

144 **ESCRTs are recruited in temporally distinct waves to the SPB extrusion site**

145 We hypothesized that Cmp7 and member(s) of the ESCRT-III family would be
146 recruited to the single NE hole generated in each fission yeast daughter cell nucleus upon
147 SPB extrusion during anaphase B (Ding et al., 1997) (Figure 1A). We therefore tested the
148 localization of functional (see Methods) GFP-tagged ESCRT proteins, including: Cmp7,
149 Vps32, Ist1, Vps24, Did4, and Did2 (Figure 1B, Supplementary Figure S1A, and
150 Supplementary Table S1) in cells co-expressing Pcp1-mCherry or Sad1-mCherry as well
151 as mCherry-Atb2 (α-tubulin) to visualize the SPB and spindle microtubules, respectively
152 (Wälde and King, 2014). By relating spindle length (mCherry-Atb2 signal) to the rate of
153 anaphase B spindle elongation (Krüger et al., 2019), we categorized anaphase B cells as
154 early (0–5 min), mid (5–7.5 min), or late (>7.5 min) to achieve greater temporal resolution.

155 We first determined the percentage of cells in each stage of the cell cycle where
156 individual GFP-ESCRTs co-localized with Pcp1-mCherry or Sad1-mCherry (Figures 1B
157 and 1C). Except for Cmp7-GFP, all GFP-ESCRTs localized to numerous cytoplasmic foci
158 that we interpret to be endosomes (Figure 1B). Consistent with the idea that ESCRTs are
159 only recruited to the NE when there is a NE hole, we rarely observed GFP-ESCRTs at
160 the SPB site in G_2-phase of the cell cycle when the NE is expected to be fully sealed
161 (Figures 1B and 1C). In contrast, except for Did2-GFP, which was never seen at the NE
162 (Supplementary Figures S1A and S1B), all other tested ESCRT fusions colocalized with
163 the SPB marker in cells from mid anaphase B to late G_1/S phases (Figures 1B and 1C),
164 which correlates with the timing of SPB extrusion from the NE (Ding et al., 1997).
165 Interestingly, the peak percentage of cells when a given GFP-ESCRT accumulated at the
166 SPB site could be temporally segregated into three waves: Cmp7 defined the first wave
167 (Mid Ana B, “Wave 1”), Vps32 and Ist1 the second (Late Ana B, “Wave 2”,), and Vps24
168 and Did4 the third (G_1/S, “Wave 3”) (Figure 1C).

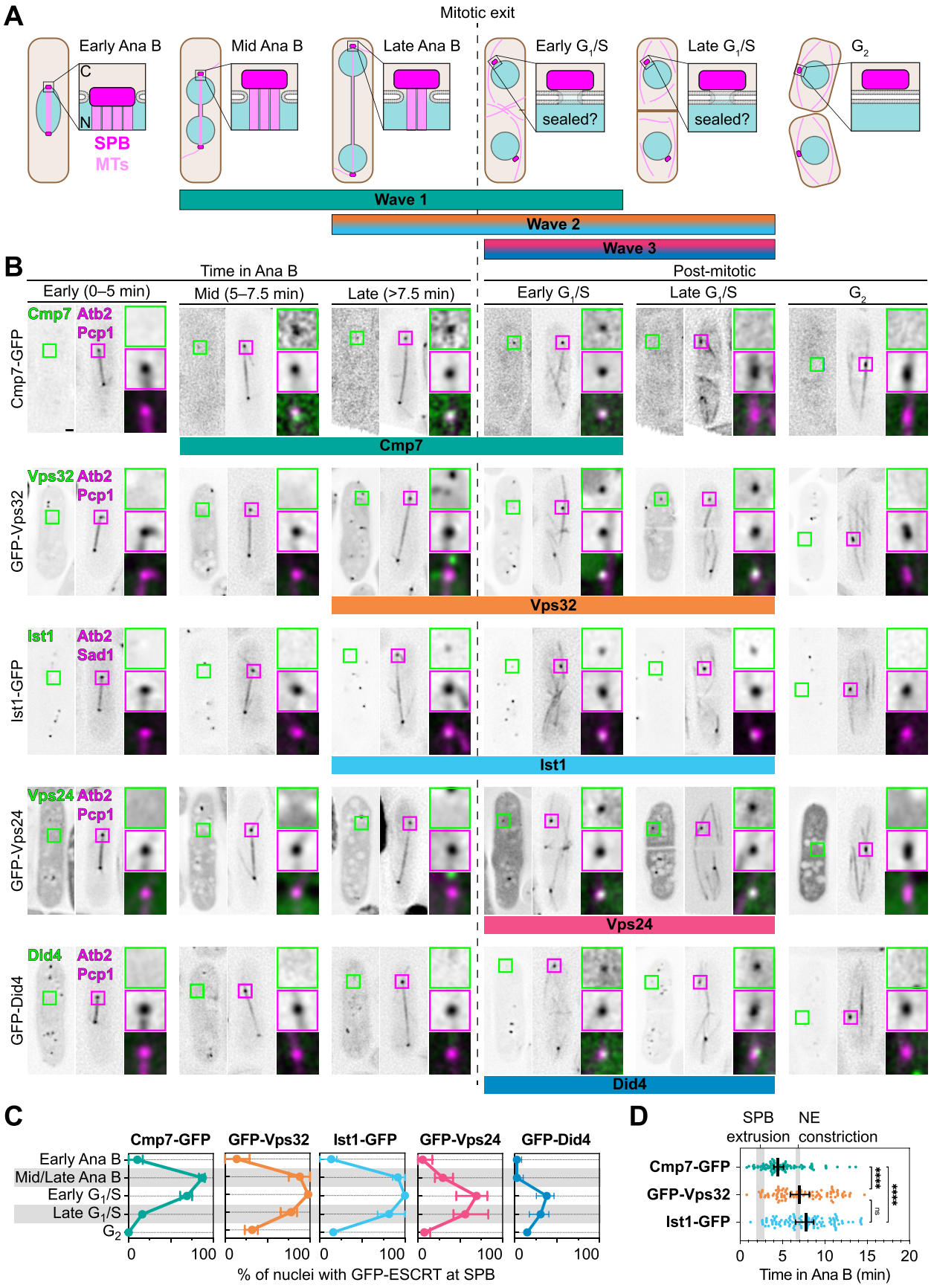
A
Mitotic exit
Early Ana B
Mid Ana B
Late Ana B
Early G1/S
Late G1/S
G2
C
N
SPB
MTs
sealed?
sealed?
Wave 1
Wave 2
Wave 3
B
Time in Ana B
Post-mitotic
Early (0–5 min)
Mid (5–7.5 min)
Late (>7.5 min)
Early G1/S
Late G1/S
G2
Cmp7-GFP
Cmp7 Atb2 Pcp1
Cmp7
GFP-Vps32
Vps32 Atb2 Pcp1
Vps32
Ist1-GFP
Ist1 Atb2 Sad1
Ist1
GFP-Vps24
Vps24 Atb2 Pcp1
Vps24
GFP-Did4
Did4 Atb2 Pcp1
Did4
C
Cmp7-GFP
GFP-Vps32
Ist1-GFP
GFP-Vps24
GFP-Did4
Early Ana B
Mid/Late Ana B
Early G1/S
Late G1/S
G2
0
100
% of nuclei with GFP-ESCRT at SPB
D
SPB extrusion
NE constriction
Cmp7-GFP
GFP-Vps32
Ist1-GFP
****
****
ns
0
5
10
15
20
Time in Ana B (min)

169

Figure 1. ESCRT proteins are recruited to the SPB extrusion site in three temporally distinct waves.

A: Diagrammatic representation of *S. pombe* cell cycle from early anaphase B through G_2 of the following cell cycle to establish the timeline in panel B. The spindle pole body (SPB) extrusion site from the nuclear envelope (NE) is magnified with the membrane architecture, if known, as described in Ding et al., 1997. N, nucleus (blue); C, cytoplasm (beige); SPB, dark magenta; microtubules (MTs), light magenta. Duration of the three waves of ESCRT recruitment observed in this study are indicated by labeled colored bars. Mitotic exit is indicated by the dotted vertical line.

B: Gallery of deconvolved, live-cell fluorescence micrographs of GFP-tagged ESCRT proteins in *S. pombe* representative of cell populations at the indicated cell cycle stages (see key in A). In each subpanel, images of the GFP-ESCRT are on left, sum projection (over 4.8 µm) of mCherry-Atb2/Pcp1-mCherry or mCherry-Atb2/Sad1-mCherry in middle and magnifications of square region of interest (ROI) shown vertically arranged at right with (top to bottom) green, magenta and merged channels. To maximize image clarity, fluorescence intensity of magnified ROIs were independently adjusted in the linear range with the exception of the magenta channel where the gamma was adjusted to 0.05 to allow visualization of mCherry-Atb2 and Pcp1-mCherry or Sad1-mCherry without saturation. Colored bars below images indicate timing of peak ESCRT recruitment in the population (see C). Scale bar, 1 µm. Magnified ROIs, 1.6 µm wide. Cmp7-GFP, MKSP3363; GFP-Vps32, MKSP3353; Ist1-GFP, MKSP3365; GFP-Vps24, MKSP3352; GFP-Did4, MKSP3334.

C: Plots of the percentage of nuclei with indicated GFP-ESCRT colocalized with SPB marker at indicated phases of the cell cycle. Points and error bars represent mean and range, respectively, across at least three biological replicates with at least 50 nuclei/GFP-ESCRT/replicate. Cmp7-GFP (MKSP3363), N = 408 nuclei; GFP-Vps32 (MKSP3353), N = 442 nuclei; Ist1-GFP (MKSP3365), N = 401 nuclei; GFP-Vps24 (MKSP3352), N = 699 nuclei; GFP-Did4 (MKSP3334), N = 623 nuclei.

D: Scatter plot where each data point represents the time in anaphase B that a GFP-ESCRT was first visible colocalized with the SPB marker across three biological replicates. Bar and error bars represent mean and standard deviation of points, respectively. Vertical gray bars indicate one standard deviation of the mean across three biological replicates for Cut11-GFP (MKSP1697) focal loss (SPB extrusion, 1.96–2.87 min) and NE constriction (6.59–7.06 min) (N = 75 cells (25 cells/replicate)). Kruskal-Wallis test performed across all datasets with Dunn's multiple comparisons across all datasets (****, $p < 0.001$; n=100; at least 17 nuclei/strain/replicate).

To further probe the relative timing of Wave 1 and Wave 2, we performed timelapse microscopy of cells progressing through mitosis expressing Cmp7-GFP, GFP-Vps32, or Ist1-GFP. We plotted the timing of the arrival (i.e., the first frame when observed) of each GFP-ESCRT at the SPB extrusion site with respect to anaphase B progression (Figure 1D). We also placed this timeline in the context of the loss of Cut11 at the SPB, which is thought to reflect SPB extrusion, and nuclear constriction into a dumbbell shape (Figure 1D, vertical grey bars) (West et al., 1998). Using this approach, we confirmed that Cmp7-GFP was recruited to the SPB site significantly earlier than GFP-Vps32 and Ist1-GFP, which were detected with similar timing (Figure 1D). Finally, to rigorously test if we could temporally segregate the Wave 1 and 2 ESCRTs in anaphase, we examined the localization of Cmp7-GFP and Ist1-mCherry within the same cell. Indeed, we found that Cmp7-GFP appeared at the SPB extrusion site prior to recruitment of Ist1-mCherry (Supplementary Figure S1C). Thus, taken together, we conclude that

183 there are three temporally distinct waves of ESCRT-III recruitment to the SPB extrusion
184 site: (1) Cmp7 in mid anaphase B, (2) Vps32/Ist1 in late anaphase B, and (3) Vsp24/Did4
185 in the subsequent G_1/S when Cmp7 departs (Figure 1A).
186
187 **ESCRT protein copy number at the SPB extrusion site**
188 With perhaps one exception (Adell et al., 2017), there remains uncertainty
189 regarding the range of numbers of ESCRT subunits required to execute a given
190 membrane fission reaction. Therefore, to inform on the organization and architecture of
191 the ESCRT polymers at the fission yeast NE, we calculated ESCRT subunit copy number
192 at the SPB extrusion site using a semi-automated ratiometric fluorescence quantification
193 approach. We directly related GFP-ESCRT fluorescence at the SPB site to kinetochore
194 foci formed by a GFP-tagged kinetochore protein, Fta3, which is found at ~37 molecules
195 per kinetochore (for details see Methods and Supplementary Figures S2A–S2C)
196 (Lawrimore et al., 2011).
197 Using the Fta3-GFP foci as standards, we quantified the average copy number of
198 all ESCRT subunits recruited to the SPB extrusion site in anaphase B and G_1/S (Table
199 1). Overall, there was an average of 16 ± 8 molecules of Cmp7-GFP per SPB extrusion
200 site. The spread in the Cmp7-GFP numbers did not reflect any change in copy number
201 during anaphase B progression or into the subsequent G_1/S-phases (Supplementary
202 Figures S2D and S2E). The Wave 2 ESCRT GFP-Vps32, regardless of mitotic stage, was
203 found at a much higher copy number of 72 ± 41 molecules (Supplementary Figures S2D
204 and S2F), suggesting an approximate 1 to 5 stoichiometry of Cmp7 to Vps32 molecules
205 at this NE hole. The Wave 3 ESCRT subunits GFP-Vps24 and GFP-Did4 were calculated
206 to be 77 ± 51 and 25 ± 10 molecules/focus, respectively (Supplementary Figure S2D).
207 The one exception to an apparently stochastic variation in ESCRT subunit copy number
208 was the Wave 2 protein Ist1-GFP, which increased in number from 25 ± 13 molecules in
209 anaphase B to 34 ± 18 into G_1/S (Supplementary Figure S2D). Consistent with an
210 increase in Ist1 copy number through anaphase B, there was a positive correlation
211 between Ist1-GFP copy number at individual NE holes with anaphase B progression

Protein	Mitotic NE hole						ILV Formation[1]
	Ana B		G_1/S		All		
	Mean ± SD	N	Mean ± SD	N	Mean ± SD	N	Mean
Cmp7	16 ± 8	88	15 ± 8	108	15 ± 8	196	*n.r.*
Vps32	75 ± 45	33	69 ± 37	35	72 ± 41	68	75–200
Ist1	25 ± 13	67	34 ± 18	80	30 ± 17	147	*n.m.*
Vps24	*n.m.*		77 ± 51	24	77 ± 51	24	15–50
Did4	*n.r.*		25 ± 10	26	25 ± 10	26	*n.m*

Table 1. Average copy number for ESCRT proteins at the NE. Copy number is shown for all examined ESCRTs by cell cycle. Copy number at intralumenal vesicle (ILV) formation at endosomes as reported in Adell et al. (2017). *n.r.,* not recruited. *n.m.,* not measured.

212 (Supplementary Figure S2G). This incremental accumulation of an ESCRT was not
213 observed for other ESCRTs in our work or that of others at ILVs (Adell et al., 2017),
214 suggesting that it could be a behavior unique to Ist1.
215
216 **Cmp7 is required for ESCRT recruitment to the NE**
217 The sequential timing of ESCRT recruitment waves to the NE suggests a
218 dependency of the later wave ESCRTs on those preceding them. To test this idea, we
219 next determined the co-dependency of ESCRT protein recruitment to the mitotic NE hole.
220 As predicted from prior work in budding yeast (Webster et al., 2016) and cultured human
221 cells (Gu et al., 2017), the recruitment of Cmp7-GFP to the SPB site required Heh1/Lem2
222 but not its paralog Heh2/Man1 (Figures 2A and 2B). Consistent with the observed
223 sequential nature of ESCRT recruitment, Wave 2 or 3 ESCRTs failed to be recruited to
224 the NE in the absence of the Wave 1 Cmp7 (Figure 2C). Thus, as has been observed in
225 other contexts (Gu et al., 2017; Olmos et al., 2016; Thaller et al., 2019; Vietri et al., 2015),
226 Cmp7 is required for all ESCRT-III recruitment to the NE.
227 We next tested the requirement of Wave 2 ESCRTs for recruitment of other GFP-
228 ESCRTs. As shown in Figure 2D, Ist1 is entirely dispensable for all GFP-ESCRT
229 recruitment to the SPB extrusion site. Interestingly, Ist1-GFP recruitment is compromised
230 but not completely abrogated in the absence of its Wave 2 partner, Vps32, appearing
231 both later and in a smaller percentage of cells compared to WT (Figure 2E). Thus,

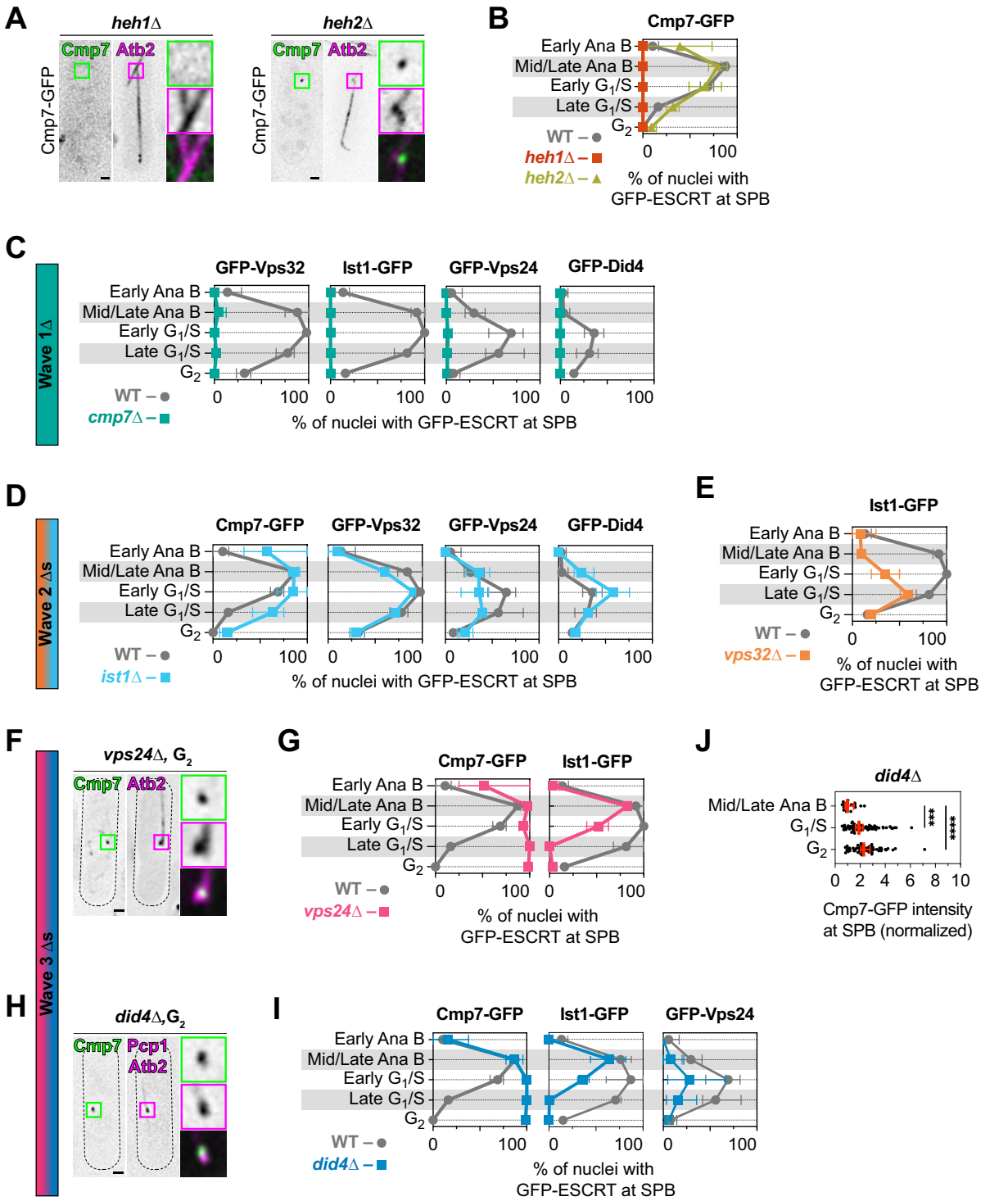

Figure 2. Cmp7 is required for ESCRT-III recruitment to the NE and is replaced by Wave 3 ESCRTs.
Figure legend continued on next page.

although Cmp7 is essential for any ESCRT-III subunit recruitment, there may not be a strict assembly order for other downstream filament assembly events.

Figure 2. Cmp7 is required for ESCRT-III recruitment to the NE and is replaced by Wave 3 ESCRTs.

A: Deconvolved fluorescence micrographs of Cmp7-GFP and mCherry-Atb2 in representative *heh1*Δ (left) and *heh2*Δ (right) cells in anaphase B. In each subpanel, images of the Cmp7-GFP are on the left, sum projection (over 4.8 µm) of mCherry-Atb2 in middle and magnifications of square ROI shown vertically arranged at right with (top to bottom) green, magenta and merged channels. Fluorescence intensity of magnified ROIs were independently adjusted in the linear range. Scale bar, 1 µm. Magnified ROIs, 1.6 µm wide.

B: Plots of the percentage of nuclei with Cmp7-GFP foci colocalized with the SPB site in WT (gray circles), *heh1*Δ (red squares), and *heh2*Δ (yellow triangles) strains in indicated phases of the cell cycle. Points and error bars represent mean and range, respectively, across at least three biological replicates with at least 50 nuclei/Cmp7-GFP/replicate. Cmp7-GFP, WT (data from Figure 1C), Cmp7-GFP, *heh1*Δ (MKSP3259), N = 203; Cmp7-GFP, *heh2*Δ (MKSP3275), N = 275 nuclei.

C: As in B but with the indicated GFP-ESCRTs in WT (gray circles) or *cmp7*Δ (green squares) cells. Points and error bars represent mean and range, respectively, across at least three biological replicates with at least 50 nuclei/GFP-ESCRT/replicate. All WT data from Figure 1C; GFP-Vps32, *cmp7*Δ (MKSP3354), N = 628 nuclei; Ist1-GFP, *cmp7*Δ (MKSP3447), N = 384 nuclei; GFP-Vps24, *cmp7*Δ (MKSP3355), N = 702 nuclei; GFP-Did4, *cmp7*Δ (MKSP3366), N = 372 nuclei.

D: As in B but with the indicated GFP-ESCRTs in WT (gray circles) or *ist1*Δ (blue squares) cells. Points and error bars represent mean and range, respectively, across at least three biological replicates with at least 50 nuclei/GFP-ESCRT/replicate. All WT data from Figure 1C; Cmp7-GFP, *ist1*Δ (MKSP3429), N = 418 nuclei; GFP-Vps32, *ist1*Δ (MKSP3449), N = 550 nuclei; GFP-Vps24, *ist1*Δ (MKSP3669), N = 323 nuclei; GFP-Did4, *ist1*Δ (MKSP3668), N = 455 nuclei.

E: As in B but with Ist1-GFP in WT (gray circles) or *vps32*Δ (orange squares) cells. Ist1-GFP, WT (data from Figure 1C), Ist1-GFP, *vps32*Δ (MKSP3504), N = 382.

F: As in A but in *vps24*Δ, G_2 cells.

G: As in B but with the indicated GFP-ESCRTs in WT (gray circles) or *vps24*Δ (red squares) cells. All WT data from Figure 1C; Cmp7-GFP, *vps24*Δ (MKSP3387), N = 236 nuclei; Ist1-GFP, *vps24*Δ (MKSP3544), N = 378 nuclei.

H: As in A but in *did4*Δ, G_2 cells. Gamma was adjusted to 0.05 to allow visualization of mCherry-Atb2 and Pcp1-mCherry without saturation.

I: As in B but with the indicated GFP-ESCRTs in WT (gray circles) or *did4*Δ (blue squares) cells. All WT data from Figure 1C; Cmp7-GFP, *did4*Δ (MKSP3381), N = 323 nuclei; Ist1-GFP, *did4*Δ (MKSP3496), N = 376 nuclei; GFP-Vps24, *did4*Δ (MKSP3511), N = 438 nuclei.

J: Plot of the fluorescence intensity of Cmp7-GFP at the SPB site in *did4*Δ cells (MKSP3381) at indicated cell cycle stages normalized to median mid/late anaphase B value for each biological replicate. Bar and error bars represent mean and standard deviation of points, respectively. Kruskal-Wallis test performed across all datasets with Dunn's multiple comparisons across all dataset (****, $p < 0.001$; N=160, at least 45 cells/replicate).

Cmp7 is replaced by Wave 3 ESCRT assemblies in G_1/S

As our temporal analysis suggests progressive remodeling of the ESCRT complement at the NE hole in concert with the cell cycle, we next tested whether the inability to recruit the final wave of ESCRTs impacted the dynamics of the upstream Wave 1 or 2 ESCRTs. Strikingly, even though the Wave 3 ESCRTs Vps24 and Did4 were found at the SPB site when the majority of Cmp7 had departed in most WT cells (Figure 1), we found that Cmp7-GFP recruitment was dysregulated in *vps24*Δ and *did4*Δ cells, remaining at the NE throughout G_1/S and even G_2 (Figures 2F–2I). Moreover, Cmp7-GFP over-

243 accumulated at the NE with mean 2-fold greater fluorescence than WT cells in *vps24*Δ
244 and *did4*Δ cells (Figure 2J). Interestingly, although the initial recruitment of the Wave 2
245 ESCRT Ist1-GFP was normal in *vps24*Δ and *did4*Δ cells, Ist1-GFP was lost earlier
246 compared to WT cells (Figures 2G and 2I). Though still observed in a small percentage
247 of SPB extrusion sites, Vps24 recruitment appeared to be largely dependent on its Wave
248 3 partner, Did4 (Figure 2I). Thus, we interpret these data in a model in which the inability
249 to complete ESCRT remodeling during G_1/S drives a reversal of the ESCRT order into an
250 aberrant Wave 1 state with persistent Cmp7-GFP recruitment.
251
252 **ESCRT waves correlate to changes in NE hole morphology**
253 To help understand ESCRT function from anaphase to G_1/S, we correlated the
254 ESCRT recruitment timeline to the ultrastructure of the NE hole at the SPB extrusion site
255 using correlative light and electron microscopy (CLEM) and electron tomography (Figure
256 3). We used Pcp1-mCherry and Cdc7-GFP, the latter of which transiently localizes to
257 mitotic/G_1 spindle poles (Sohrmann et al., 1998), to help inform the location of the SPB
258 extrusion site and the cell cycle stage of embedded cells. At the correlated location of
259 these SPB markers, we identified the SPB plaques as an electron-dense region in the
260 cytoplasm apposing the nucleus from early anaphase B to G_2 (Figures 3A–3D, red
261 outline). We also observed an electron-lucent region of cytosol surrounding the SPB
262 plaques that excluded ribosomes (Figures 3A–D, orange outline).
263 The onset of the Wave 1 ESCRT recruitment occurs in mid anaphase B; in all cells
264 examined that corresponded to early/mid anaphase B, there was a 78 to 182 nm (median,
265 140 nm) wide (Figure 3I, n=10) fenestration in the NE apposing the SPB (Figure 3A, black
266 arrowhead); spindle microtubules were visible passing through this hole in select virtual
267 slices of the entire tomogram (Movie 1). Interestingly, we observed a marked narrowing
268 of the diameter of the NE hole to 14 to 115 nm (median, 59 nm) (Figure 3I, n=5) in late
269 anaphase B cells, alongside a reduction in the number of microtubules (Figure 3B, black
270 arrowhead) (Movie 2) (Ding et al., 1997). These data suggest that the recruitment of the
271 Wave 2 ESCRTs temporally correlates with a constriction of the NE hole from ~140 to
272 ~60 nm. Subsequently, in G_1/S cells we found either relaxation of the NE hole (26 to 228
273 nm; median, 184 nm; 4/7 analyzed; Figures 3C, black arrowhead and 3I) or cells that had

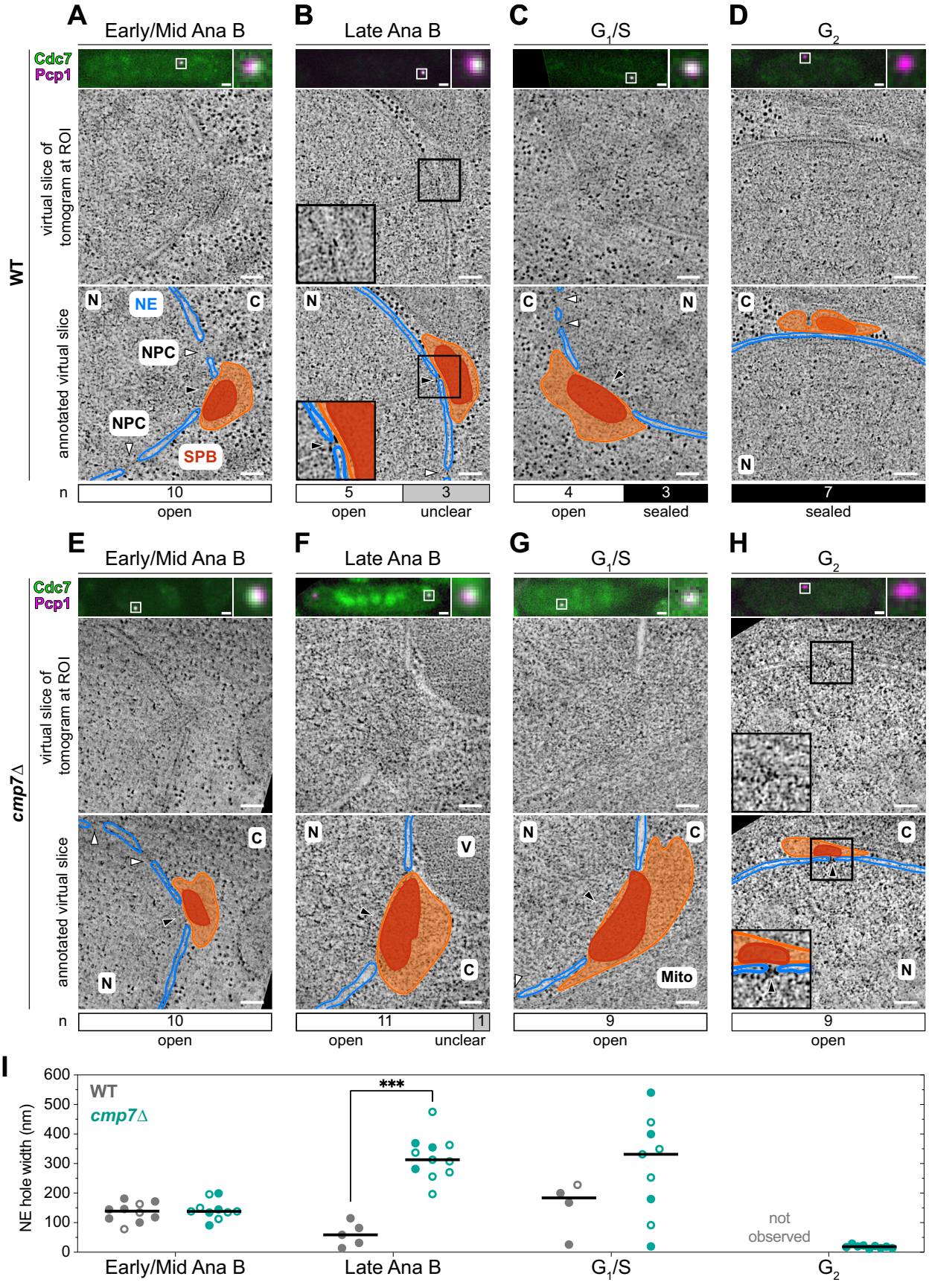
A
Early/Mid Ana B
B
Late Ana B
C
G1/S
D
G2
Cdc7
Pcp1
WT
virtual slice of tomogram at ROI
annotated virtual slice
N
NE
C
NPC
NPC
SPB
n
10
open
5
3
open
unclear
4
3
open
sealed
7
sealed
E
Early/Mid Ana B
F
Late Ana B
G
G1/S
H
G2
cmp7Δ
V
Mito
11
1
9
9
I
NE hole width (nm)
600
500
400
300
200
100
0
WT
cmp7Δ
***
not observed
Early/Mid Ana B
Late Ana B
G1/S
G2

274

Figure 3. Cmp7 is required to restrict the size of the NE hole in anaphase and seal the NE in G_1/S.

A–D: Top, fluorescence micrograph of a thick section of a resin-embedded yeast strain (MKSP3180) expressing Cdc7-GFP (green) and Pcp1-mCherry (magenta) prepared for correlative light and electron microscopy (CLEM) and electron tomography (ET). The indicated cell cycle stages were determined by a combination of fluorescence marker presence/localization and ultrastructural features. The white square in the fluorescence micrographs indicates regions where the electron tomogram was collected and is shown magnified at the right. Middle and bottom panels are a virtual slice taken from the electron tomogram shown without (middle) and with (bottom) manual annotation of features. NE, blue, SPB plaques, red, electron-lucent ribosome exclusion zone extending beyond SPB plaques, orange. White arrowheads, NPC. Black arrowheads, SPB extrusion hole. N, nucleus; C, cytoplasm. Scale bars: fluorescence micrographs, 1 µm; virtual slices from electron tomogram, 100 nm.

E–H: CLEM and ET for *cmp7*Δ cells (MKSP3243), prepared and displayed as in A. Mito, mitochondria; V, vacuole.

I: Scatter plot of NE hole widths in tomograms of WT (gray circles) and *cmp7*Δ (green circles). Solid circles represent exactly determined diameters while open circles represent minimum values in cases where the full diameter was not visualized in the volume. Black bars represent median. Mann-Whitney test performed between WT and *cmp7*Δ for each cell cycle phase individually (***, $p < 0.0001$; all others, $p \geq 0.05$). WT cells, MKSP3180, N = 14 nuclei; *cmp7*Δ cells, MKSP3243, N = 39 nuclei.

completed NE sealing (3/7 analyzed), suggesting that the timing of Wave 3 corresponds to the act of NE sealing. Consistent with this interpretation, the NE membranes were continuous in all 7 G_2-phase cells examined (Figures 3D and 3I). Thus, each wave of ESCRT recruitment corresponds to distinct morphological changes of the NE hole; Wave 2 corresponds to a transient NE constriction while Wave 3 represents a timepoint that is suggestive of a role in NE sealing.

ESCRTs restrict the size of the NE hole during mitosis

To directly evaluate whether ESCRTs impact the observed NE hole dynamics, we performed CLEM on *cmp7*Δ cells, which fail to recruit all ESCRT-III proteins (Figure 2C). Loss of *CMP7* did not impact the morphology or diameter of the NE fenestration in early/mid anaphase B cells, which appeared similar to WT in all cells examined (n=10; Figures 3A, 3E, and 3I; Movie 3). In striking contrast, late anaphase B *cmp7*Δ cells (n=12) exhibited massive NE gaps ranging from 197 to 475 nm (median, 313 nm) (Figures 3F and 3I; Movie 4), an approximate five-fold increase compared to WT cells at the same stage (Figures 3B and 3I). Thus, we conclude that Cmp7 is required to restrict the diameter of the mitotic NE hole during anaphase B. Given that this state temporally precedes the recruitment of Wave 3 ESCRTs (Figure 1), this function in restricting the size of the NE hole in late anaphase B likely represents a state comprised of Wave 1 and Wave 2 ESCRTs.

295

296 **Cmp7 is required to complete NE sealing but must be remodeled to Wave 3 ESCRTs**

297 Interestingly, in G_1/S when WT NE holes had either been sealed or persisted with
298 a width of 26 to 288 nm (median, 184 nm), NE gaps were observed in all imaged *cmp7*Δ
299 cells and displayed a larger range from 20 to 540 nm (median, 332 nm; n=6, Figures 3G
300 and 3I). Although not statistically different, the large spread of values in individual *cmp7*Δ
301 cells suggests that the aberrantly large fenestrations arising in anaphase B might persist
302 into the subsequent G_1/S. Most strikingly, G_2 *cmp7*Δ cells (n=9, Figure 3H) all retained a
303 discernable but small NE fenestration with a range of diameters from 14 to 29 nm
304 (median, 19 nm; Figure 3I), suggesting that an ESCRT-independent mechanism
305 ultimately constricted, but failed to seal, the NE fenestration.

306 As our light microscopy data demonstrated that Cmp7 aberrantly persists in cells
307 lacking Wave 3 ESCRTs (Figures 2F–2J), we also interrogated the morphological
308 consequences of reversion to an aberrant Wave 1 assembly state by applying CLEM and
309 electron tomography to G_2 *did4*Δ cells (Figures 4A and 4B). At the majority (8/13) of
310 Cmp7-GFP NE foci we selected, we correlated the fluorescence to an 8 to 34 nm (median,
311 21 nm) hole in the NE (Figure 4C), suggesting that the persistent Wave 1 state also
312 disrupts NE sealing; in the other 5 samples, we could not unambiguously observe a NE
313 hole (Figures 4A and 4B). Unlike in *cmp7*Δ cells, however, in *did4*Δ cells we found that
314 the persistent NE hole was filled with densely stained material (Figure 4A), which we
315 interpret to be Cmp7-GFP, although other, yet to be defined factors may also be present.
316 Interestingly, although Cmp7-GFP persisted at the SPB extrusion site throughout G_2 in
317 *did4*Δ cells, it began to disappear at the time of the subsequent SPB insertion cycle
318 (Figure 4D). These data suggest a mechanism to "reset" the SPB site for another round
319 of SPB insertion, extrusion and NE sealing that might entail clearing aberrant ESCRT
320 assemblies from the NE. Thus, we conclude that Cmp7's role in initiating ESCRT-III
321 assembly is required to close the constricted, 20 nm NE fenestration in G_2. Moreover, the
322 loss of Wave 3 ESCRTs leads to the accumulation of Cmp7 in NE holes that fail to seal,
323 highlighting that it is the replacement of the initial Wave 1/Wave 2 ESCRT assemblies to
324 the Wave 3 ESCRT state that ultimately drives the sealing reaction.

325

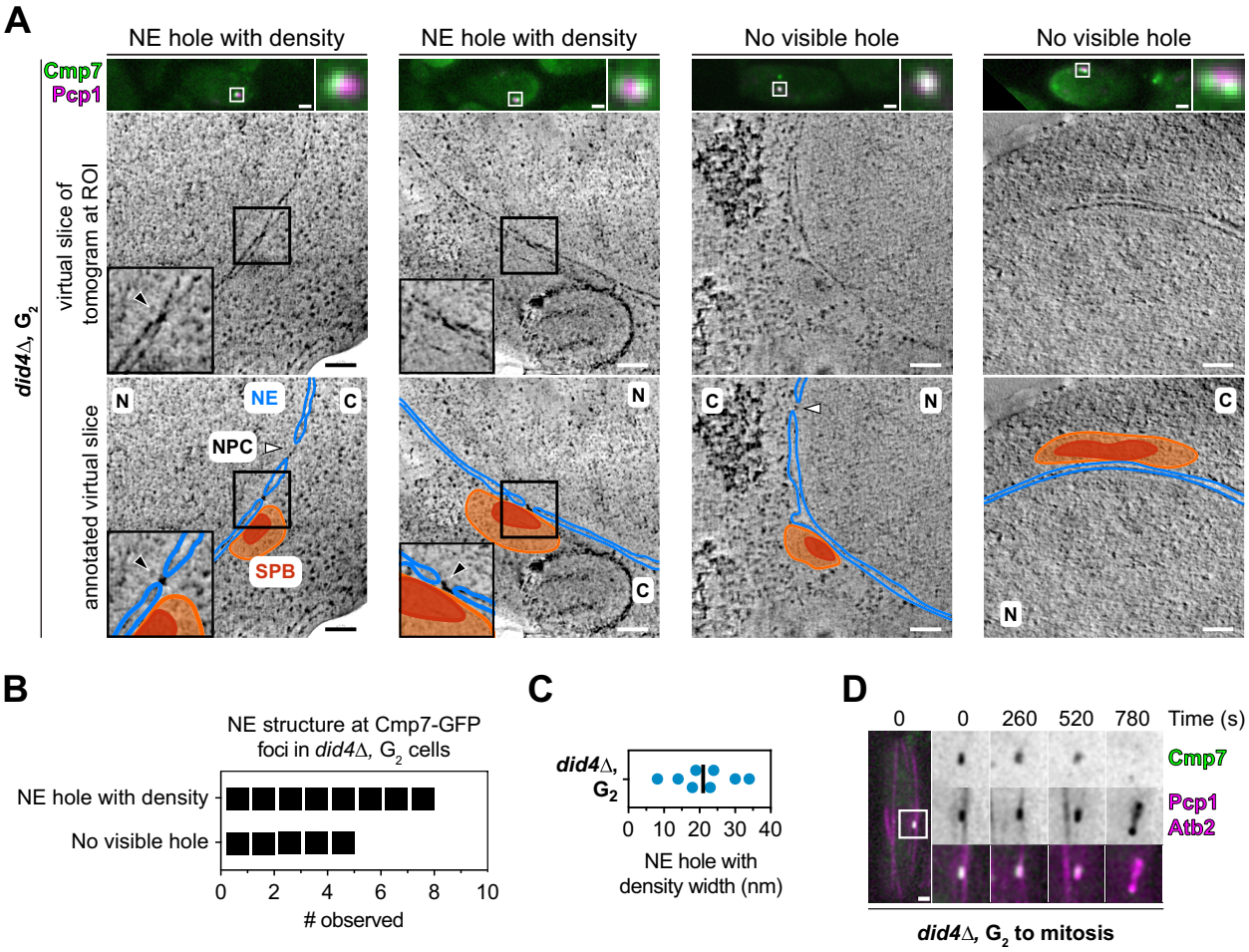

326

Figure 4. Did4 is required to remove Cmp7 to seal the NE.

A: Gallery of four representative electron tomograms showing either NE holes filled with electron density (left) or no visible NE holes (right). In each sub panel: Top, fluorescence micrograph of a thick section of a resin-embedded *did4*Δ strain (MKSP3381) in G_2 expressing Cmp7-GFP (green) and Pcp1-mCherry (magenta) prepared for CLEM and ET. The white square in the fluorescence micrographs indicates the region where the electron tomogram was collected and is shown magnified at right. Middle and bottom panels are a virtual slice taken from the electron tomogram shown without (middle) and with (bottom) manual annotation of features. NE, blue, SPB plaques, red, electron-lucent ribosome exclusion zone extending beyond SPB plaques, orange. White arrowheads, NPC. Black arrowheads, NE hole with density. N, nucleus; C, cytoplasm. Scale bars: fluorescence micrographs, 1 µm; virtual slices from electron tomogram, 100 nm.

B: Plot of the number of occurrences (black squares) of the observed NE phenotypes from A. MKSP3381, N = 13 nuclei.

C: Scatter plot of NE hole widths (nm) observed in *did4*Δ, G_2 cell tomograms as in A. Black bar represents median. MKSP3381, N = 8 nuclei.

D: Deconvolved fluorescence micrographs of a timelapse series (top, seconds representing the transition from G_2 into mitosis) of a *did4*Δ cell expressing Cmp7-GFP (green), Pcp1-mCherry (magenta), and mCherry-Atb2 (magenta). The white square in the overview micrograph indicates the ROI magnified in the image series vertically arranged at right with (top to bottom) green, magenta and merged channels. Representative cell (MKSP3381) from three biological replicates of imaging N = 180 cells, at least 60 cells/replicate.

327 **Although required for NE sealing, Cmp7 is dispensable for maintaining the nuclear**
328 **compartment**
329 The persistence of NE holes at the SPB extrusion site throughout the cell cycle in
330 *cmp7*Δ cells, and in particular the massive NE fenestrations observed during mitosis,
331 prompted an evaluation of nucleocytoplasmic compartmentalization in these conditions.
332 We tested the distribution of GFP fused to either three (MGM2) or five (MGM4) maltose-
333 binding proteins; while MGM2 is able to diffuse across NPCs, the larger MGM4 construct
334 is effectively excluded from the nucleus (Figure 5A and Supplementary Figure S3A)
335 (Popken et al., 2015). Consistent with this, most MGM2 cells had nuclear to cytoplasmic
336 ratios (N/C ratios) >0.75 and most MGM4 cells had N/C ratios <0.75; we therefore used
337 N/C ratio = 0.75 as a cut-off to gauge whether cells expressing MGM4 displayed a defect
338 in their nucleocytoplasmic compartmentalization (Supplementary Figure S3A). Using this
339 framework, we found that *cmp7*Δ cells displayed no detectable loss of nuclear
340 compartmentalization, consistent with prior work (Gu et al., 2017) (Figure 5A).
341
342 **Cmp7 cooperates with a diffusion barrier to maintain the nuclear compartment**
343 The observation that deletion of *CMP7* did not appreciably impact
344 nucleocytoplasmic compartmentalization despite the presence of large NE fenestrations
345 was, on the surface, surprising. It should be considered, however, that even in WT cells
346 there is a period (~14 minutes) after SPB extrusion when the nuclear compartment
347 appears intact despite the presence of a NE fenestration of at least ~60 nm but up to 228
348 nm beneath the SPB (Figure 3). Thus, there must be additional, unidentified diffusion
349 barrier(s) (beyond the NPC) capable of maintaining nucleocytoplasmic
350 compartmentalization in the face of a persistent NE hole. To test this idea, we employed
351 1,6-hexanediol (1,6-HD), an aliphatic alcohol that disrupts weak hydrophobic protein-
352 protein interactions underlying biomolecular condensation including that of FG-repeat
353 containing nucleoporins that contribute to the NPC diffusion barrier (Ribbeck and Görlich,
354 2002; Shulga and Goldfarb, 2003). We observed that 5%, but not 2.5%, 1,6-HD treatment
355 led to the equilibration of MGM4 fluorescence across the NE in about 20 minutes in WT
356 G_2 cells (Figures 5B and 5C), indicating disruption of the NPC diffusion

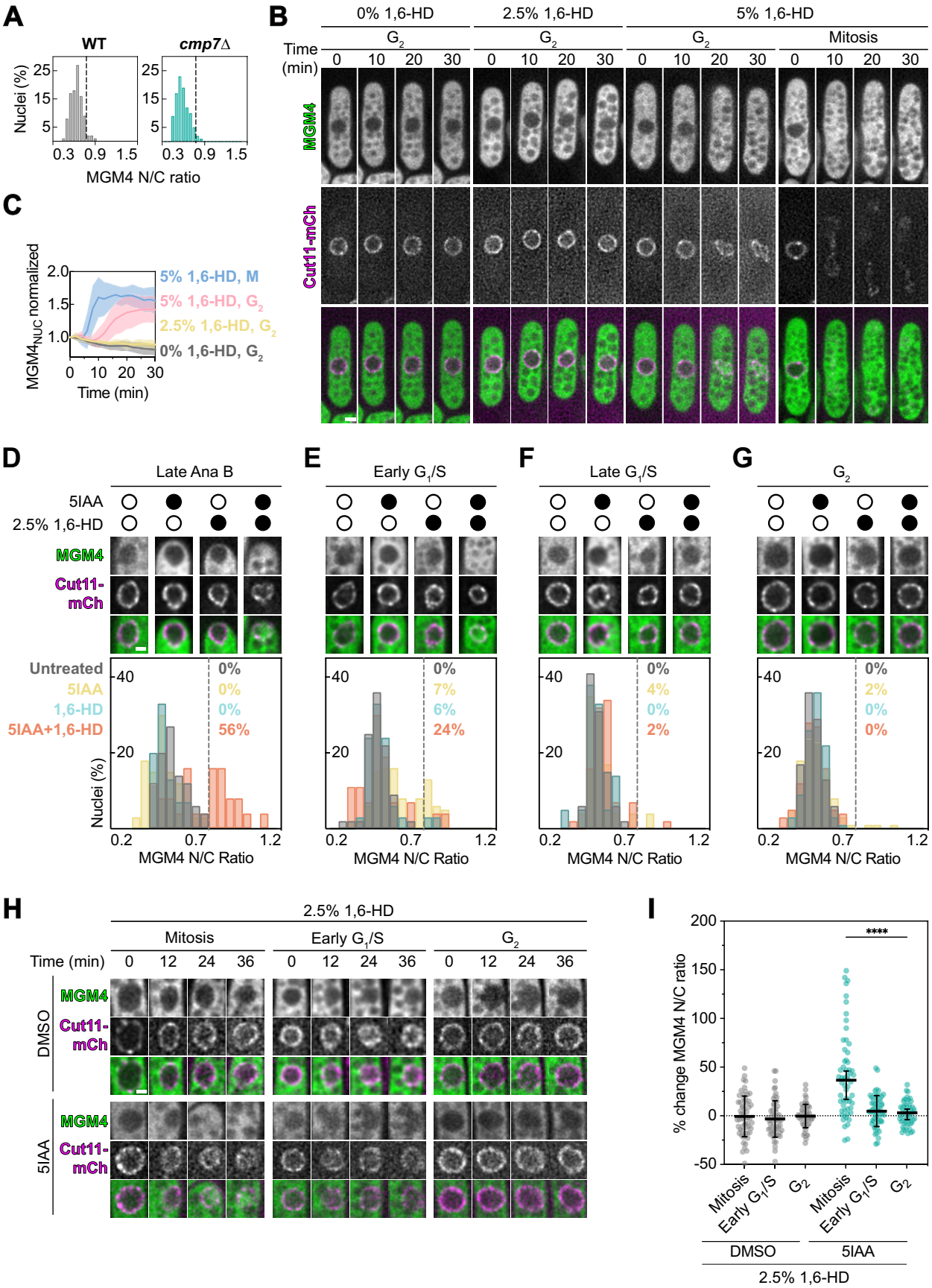
A
WT
cmp7Δ
Nuclei (%)
MGM4 N/C ratio
B
0% 1,6-HD
2.5% 1,6-HD
5% 1,6-HD
G2
Mitosis
Time (min)
MGM4
Cut11-mCh
C
MGM4NUC normalized
5% 1,6-HD, M
5% 1,6-HD, G2
2.5% 1,6-HD, G2
0% 1,6-HD, G2
Time (min)
D
Late Ana B
E
Early G1/S
F
Late G1/S
G
G2
5IAA
2.5% 1,6-HD
Untreated
5IAA
1,6-HD
5IAA+1,6-HD
MGM4 N/C Ratio
H
2.5% 1,6-HD
Mitosis
Early G1/S
DMSO
5IAA
I
% change MGM4 N/C ratio
****
Mitosis
Early G1/S
G2
DMSO
5IAA
2.5% 1,6-HD

Figure 5. Cmp7 and a 1,6 hexanediol-sensitive diffusion barrier ensure nucleocytoplasmic compartmentalization during mitosis.

A: Histogram relating nucleoplasmic and cytoplasmic GFP fluorescence of MGM4 in a N/C ratio of individual WT and *cmp7*Δ cells across three biological replicates. Size between bins, 0.05. Dotted line at 0.75 bin. WT (MKSP3345 and MKSP3488), N = 240 nuclei; *cmp7*Δ (MKSP3535), N= 177 nuclei.

B: A time-lapse series of deconvolved fluorescence micrographs of cells (MKSP3699) expressing MGM4 and Cut11-mCherry (Cut11-mCh). Green (top), magenta (middle) and merged image (bottom) shown. Cells were treated with 0%, 2.5% or 5% 1,6-hexanediol (1,6-HD) as indicated. For G_2 cells, time 0 indicates the start of imaging after the delivery of 1,6-HD by microfluidics. For mitotic cells, only cells that went through mitosis after 1,6-HD treatment were considered. Across the population, the constriction of the NE into a dumbbell shape (~10 min) was used to align individual traces in C. Scale bar, 1 µm. Representative of 20 cells per condition with at least 5 cells per condition for each of three biological replicates.

C: Plot of the nuclear (NUC) fluorescence of MGM4 through timelapse imaging experiments as shown in B normalized to the initial timepoint for each individual nucleus of a cell (MKSP3699, untreated). Solid lines represent average of 20 cells per condition with at least 5 cells per condition for each of three biological replicates, with the shaded region representing the standard deviation. M = mitosis.

D–G: Asynchronous cells (MKSP3699) expressing MGM4, Cut11-mCherry (Cut11-mCh), Cmp7-AID and OsTIR1$_{F74A}$ were treated for 1 h with DMSO or 5-adamantyl-IAA (5IAA) followed by EMM5S media with or without 2.5% 1,6-HD—treatments indicated by closed circles—before imaging. Post-imaging, cells were categorized by cell cycle stage and analyzed. At the top of each panel are representative images of an ROI that encompasses a nucleus with MGM4, Cut11-mCh and merged images arranged vertically. Scale bar, 1 µm. At bottom, histograms of N/C ratios of MGM4 fluorescence of individual cells in untreated (gray), 5IAA (yellow), 2.5% 1,6-HD (teal), and both 5IAA and 2.5% 1,6-HD (orange). Percent of values above 0.75 bin (dotted gray line) for each reporter indicated. Size between bins, 0.05. Quantification was performed for three biological replicates N = 955, with at least 197 cells/condition, and at least 50 cells/biological replicate.

H: DMSO or 5IAA-treated cells (MKSP3699) at indicated cell cycle stages expressing MGM4, Cut11-mCherry (Cut11-mCh), Cmp7-AID and OsTIR1$_{F74A}$ were subjected to timelapse imaging after the addition of 2.5% 1,6 HD delivered by microfluidics. For G_2 and G_1/S cells, time 0 indicates the start of imaging after the delivery of 1,6-HD by microfluidics. For mitotic cells, only cells that went through mitosis after 1,6-HD treatment were considered. Images of representative nuclei at each timepoint are shown arranged vertically with MGM4 (green) at top, Cut11-mCherry (Cut11-mCh; magenta) in middle and merge at bottom. Scale bar, 1 µm. Representative of N=360, 20 cells/replicate/cell cycle phase/treatment.

I: Scatterplot of the percent change of MGM4 N/C ratios of individual cells (MKSP3699, either DMSO or 5IAA-treated) expressing MGM4, Cut11-mCherry, Cmp7-AID and OsTIR1$_{F74A}$ from start to end of timelapse imaging after addition of 2.5% 1-6 HD. Bars and error bars represent mean and standard deviation, respectively. Kruskal-Wallis test performed across all cell cycle phases with Dunn's multiple comparisons for each data set against G_2 for the corresponding treatment (****, $p < 0.0001$; ns, $p \geq 0.05$). N=360, 20 cells/replicate/cell cycle phase/treatment.

358 barrier. Interestingly, MGM4 fluorescence equilibrated approximately twice as fast in
359 mitotic cells (Figures 5B and 5C). This observation hints that either the NPC diffusion
360 barrier is weakened during mitosis or there is an additional proteinaceous NE diffusion
361 barrier required during mitosis that is also sensitive to 5% 1,6-HD.

362 Building on a model where there is a mitotic-specific NE diffusion barrier, we
363 reasoned that such a barrier would be vulnerable to the loss of Cmp7, which leads to a
364 much larger NE hole in anaphase B (Figures 3F and 3I). To test this, we turned to an
365 auxin-induced degron (AID) system to quickly deplete an endogenously expressed
366 Cmp7-AID fusion, which allowed us to specifically test the impact of the loss of Cmp7

367 during mitosis (Kanke et al., 2011; Zhang et al., 2022). Cmp7-AID was efficiently
368 degraded within 15 minutes of treatment with 5-adamantyl-IAA (5IAA) (Supplementary
369 Figure S3B). Importantly, depletion of Cmp7-AID recapitulates phenotypes observed in
370 *cmp7Δ* cells, for example abolishing recruitment of Ist1-GFP to the NE (Supplementary
371 Figure S3C). Further, like *cmp7Δ*, there was no discernable change in MGM4 N/C
372 fluorescence ratios in 5IAA-treated Cmp7-AID cells (Figures 5D–5G).
373 We therefore sought to specifically disrupt the putative mitotic diffusion barrier in
374 Cmp7-AID depleted cells with 2.5% 1,6-HD, which is insufficient to disrupt the NPC
375 diffusion barrier even during mitosis (Figures 5B–5D, and 5H). Strikingly, treatment of
376 Cmp7-AID depleted cells with 2.5% 1,6-HD resulted in nuclear entry of MGM4 in 56% of
377 late anaphase B cells and 24% of early G_1/S cells but did not impact MGM4 distribution
378 in G_2 cells (Figures 5D–5G). To confirm that the nuclear entry of MGM4 occurred
379 specifically during mitosis under conditions of Cmp7 depletion, we monitored MGM4
380 localization in Cmp7-AID cells (with or without 5IAA) alongside the temporally controlled
381 delivery of 2.5% 1,6-HD in a microfluidic chamber (Figures 5H and 5I). As shown in Figure
382 5H, only mitotic cells depleted of Cmp7-AID in the presence of 2.5% 1,6-HD allowed entry
383 of MGM4 into the nucleus, which we quantified as the percent change in N/C fluorescence
384 ratios of individual cells from the beginning to the end of the experiment (Figure 5I).
385 Together, these data suggest that Cmp7 supports a mitotic diffusion barrier independent
386 of NPCs that is distinct from its role in NE membrane sealing.
387
388 ***CMP7* and *HEH1* genetically interact with genes encoding SPB components**
389 We next sought to identify the protein(s) that help form a diffusion barrier capable
390 of preventing macromolecules from transiting a NE hole as large as ~500 nm. Based on
391 the CLEM data, which showed the SPB and a zone of ribosome exclusion covering even
392 the largest NE holes in *cmp7*Δ cells (Figure 3), SPB components were the most likely
393 candidates. We therefore considered the possibility that the observed zone of ribosome
394 exclusion is analogous to the pericentriolar material that surrounds mammalian
395 centrosomes. A key evolutionarily conserved component of the pericentriolar material is
396 pericentrin (Pcp1), which is an attractive candidate to form a diffusion barrier because it
397 is capable of undergoing biomolecular condensation and may be sensitive to 1,6-HD

398 (Jiang et al., 2021). To begin to explore this hypothesis, we tested genetic interactions
399 between *CMP7* and *HEH1* with *PCP1* (Figures 6A and 6B). As *PCP1* is essential for
400 viability, we took advantage of strains expressing two temperature sensitive alleles, *pcp1-*
401 *15* and *pcp1-18,* that inhibit growth at 36 ˚C (Fong et al., 2010). As shown in Figures 6A
402 and B, when grown at the permissive growth temperatures (25˚C and 32˚C), *cmp7Δpcp1-*
403 *18* and *heh1Δpcp1-18* strains produced colonies of smaller size compared to their
404 parental counterparts, suggesting a functional relationship between Pcp1 and the
405 recruitment of Cmp7 to the SPB extrusion site.
406 Building upon this, we also tested whether there was a genetic interaction between
407 the gene encoding the KASH-domain protein, Kms2, which is thought to anchor the SPB
408 to the NE (Wälde and King, 2014) and *CMP7* or *HEH1*. We used a strain expressing a
409 conditional knockdown allele of *KMS2* that is depleted in media containing thiamine,
410 *Pnmt81:kms2 DAmP* (*kms2 DamP*) (Wälde and King, 2014). Although we detected a mild
411 loss of fitness in *cmp7Δkms2 DamP* cells at 25˚C (Figure 6A), the growth defect of the
412 *heh1Δkms2 DamP* strain was more severe, particularly at 32˚C, where the combination
413 was lethal (Figure 6B). Cumulatively, our data suggest that Cmp7 and Heh1 are required
414 for the fitness of cells whose SPBs are compromised or are defective at SPB anchoring
415 to the NE; Heh1 might also have additional roles beyond simply recruiting Cmp7 to the
416 NE that might explain the greater dependence of the *kms2 DamP* allele on its presence.
417
418 **Pcp1 supports a mitotic diffusion barrier**
419 We next sought to investigate if the loss of fitness of *cmp7Δpcp1-15/18* cells could
420 be attributed to a specific disruption of a mitotic NE diffusion barrier. To address this, we
421 analyzed the distribution of MGM4 in *pcp1-15* and *cmp7Δpcp1-15* cells grown at 30˚C
422 and then either imaged directly (0 h) or following 3 h at 36˚C (Figure 6C). At the permissive
423 temperature of 30˚C, there was little change in MGM4 N/C fluorescence ratios in either
424 strain at any cell cycle stage (Figures 6C and 6D). However, following 3 h at 36˚C, we
425 observed that *cmp7Δpcp1-15* cells had an increase in nuclear MGM4 fluorescence with
426 N/C ratios >0.75 that was particularly evident in G_1/S cells (65%). As 20% of *pcp1-15*
427 cells also showed a loss of nucleocytoplasmic compartmentalization in G_1/S (Figure 6D),
428 we interpret these data as evidence that Pcp1 establishes and/or maintains a NE diffusion

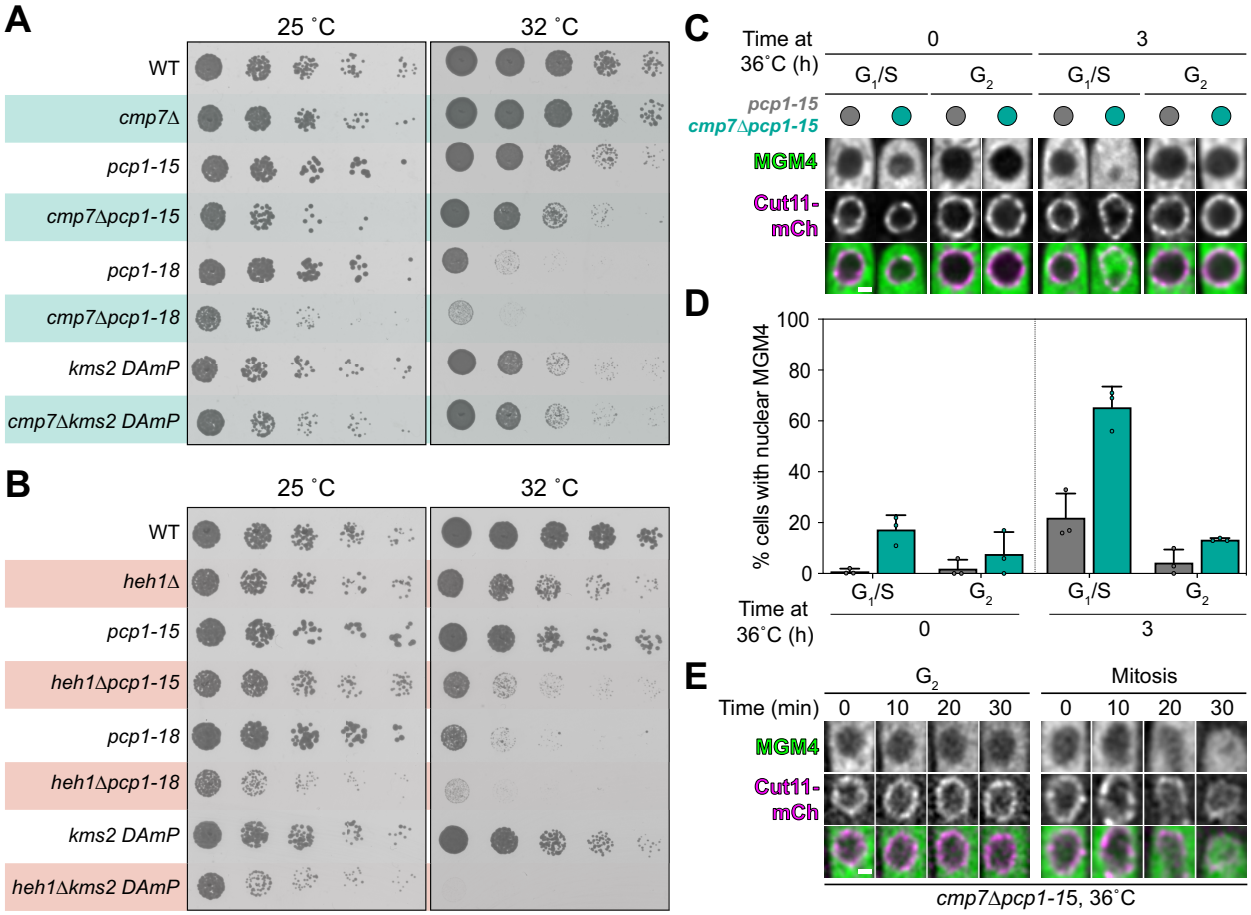

429

Figure 6. *CMP7* and *HEH1* interact with genes encoding SPB components; Pcp1 is required to maintain nuclear integrity in the absence of *CMP7*

A, B: The indicated strains were serially diluted 10-fold and plated on YE5S plates incubated at the indicated temperatures. Plates were imaged after 2 days (32˚C) or 5 days (25˚C). Images are representative of 3 biological replicates. WT, MKSP399; *cmp7Δ*, MKSP3340; *pcp1-15*, MKSP280; *cmp7Δpcp1-15*, MKSP3420; *pcp1-18*, MKSP281; *cmp7Δpcp1-18*, MKSP3425; *kms2 DAmP*, MKSP1474; *cmp7Δkms2 DAmP*, MKSP3683; *heh1Δ*, MKSP3248; *heh1Δpcp1-15*, MKSP3838; *heh1Δpcp1-15*, MKSP3839; *heh1Δkms2 DAmP*, MKSP3843.

C: Fluorescence micrographs of representative nuclei are shown arranged vertically with MGM4 (green) at top, Cut11-mCherry (Cut11-mCh; magenta) in middle and merge at bottom in either *pcp1-15* (gray circle, MKSP3812) or *cmp7Δpcp1-15* (green circle, MKSP3811) strains. Cells were grown at 30˚C then imaged directly (0 h) or following 3 h at 36˚C (3 h). Scale bar, 1 µm.

D: Plot of the percentage of *pcp1-15* (gray bar, MKSP3812) or *cmp7Δpcp1-15* (green bar, MKSP3811) MGM4-expressing cells with N/C fluorescence ratios greater than 0.75 reflecting a loss of nuclear integrity. Points are the mean from each biological replicate, while bars and error bars represent total mean and standard deviation, respectively. Points represent average of at least 30 nuclei/cell cycle phase/strain/replicate, N = 977.

E: Fluorescence micrographs of representative nuclei are shown arranged vertically with MGM4 (green) at top, Cut11-mCherry (Cut11-mCh; magenta) in middle and merge at bottom from individual *cmp7Δpcp1-15* cells (MKSP3811) in G_2 or through a timecourse (in minutes) after a temperature shift from 30˚C to 36˚C. MGM4 (top), Cut11-mCh (middle) and merge (bottom) shown. Scale bar, 1 µm.

430 barrier that is more susceptible to disruption in cells lacking Cmp7. To confirm that the
431 nuclear entry of MGM4 in G_1/S cells occurred specifically during mitosis, we performed

432 timelapse imaging of *cmp7Δpcp1-15* cells during a temperature shift from 30˚C to 36˚C.
433 Strikingly, the overwhelming majority of cells (91%, N=75) that leaked MGM4 into the
434 nucleus during this timecourse were undergoing mitosis (Figure 6E). Thus, Cmp7 is
435 required to support the integrity of a Pcp1-dependent NE diffusion barrier that functions
436 during mitosis. Moreover, these data further demonstrate that NPCs are not the sole NE
437 diffusion barrier.
438

DISCUSSION

Here we develop and exploit the fission yeast *S. pombe* as a model of ESCRT function at the NE (Supplementary Figure S4). The data firmly establish that ESCRTs are required to seal the NE hole generated by the extrusion of the SPB. Critically, however, we also propose a new function for ESCRTs prior to sealing in which they act as a molecular grommet that restricts the size of the persistent NE fenestration during anaphase B. This grommet function is needed to support a proteinaceous diffusion barrier that is essential to maintain nucleocytoplasmic compartmentalization. Thus, in addition to extending the functional repertoire of ESCRTs, we also introduce the exciting concept that, beyond the NPC, there are other protein diffusion barriers that restrict the passage of macromolecules across the NE.

Our data from fission yeast highlight a broader theme, together with published work, in which ESCRTs and proteinaceous diffusion barriers act in concert to protect the integrity of the nuclear compartment. A clear corollary, for example, is how the NPC diffusion barrier installed during NPC biogenesis is supported by the ESCRT pathway in the event that NPC biogenesis fails (Thaller et al., 2019; Thaller et al., 2021; Webster et al., 2014; Webster et al., 2016). Another example might include the rapid recruitment of barrier to autointegration factor (BAF) to exposed chromatin at induced NE ruptures (Halfmann et al., 2019). As BAF forms a cross-linked network that can restrict the passage of macromolecules 500 kDa/49 nm in size (Samwer et al., 2017), it is possible BAF together with other factors (including lamin C (Kono et al., 2022)) might plug NE holes quickly before the membranes themselves are later sealed through a mechanism involving LEM protein(s) and ESCRTs. A similar function could be served by galectin, which appears capable of forming biomolecular condensates (Chiu et al., 2020) and recruiting ESCRT-III (Jia et al., 2020) to prevent leakage of lysosomal hydrolases during ESCRT repair of lysosome membranes (Radulovic et al., 2018; Skowyra et al., 2018).

In the case of fission yeast, we identify the ortholog of the pericentriolar material protein pericentrin, Pcp1, as key to supporting the diffusion barrier that acts in concert with the ESCRT grommet at the NE in mitosis (Figure 6). We think the most likely physiochemical mechanism underlying the formation of a Pcp1-dependent diffusion barrier is biomolecular condensation. First, there is clear precedence for phase-separated

470 condensates forming selective barriers at the NE including the FG-nucleoporins of the
471 NPC (Celetti et al., 2020; Frey et al., 2006; Petri et al., 2012). Second, the SPB of budding
472 yeast is constitutively inserted in the NE (Byers and Goetsch, 1975; O'Toole et al., 1999)
473 while the nuclear compartment is defined by NPCs, suggesting that the ability of SPB
474 components to restrict the diffusion of macromolecules is a fundamental property of these
475 structures across divergent yeasts. Third, the Pcp1-dependent mitotic barrier described
476 here is, like many biomolecular condensates, sensitive to perturbation by relatively low
477 concentrations of 1,6-HD (Figure 5) (Ribbeck and Görlich, 2002; Shulga and Goldfarb,
478 2003). Fourth, we previously demonstrated that Pcp1 molecules incorporated into the
479 SPB undergo little to no turnover with the soluble Pcp1 pool (Wälde and King, 2014),
480 behaving essentially as a solid material, consistent with its ability to undergo biomolecular
481 condensation. Fifth, the ability of the orthologous pericentrin to undergo biomolecular
482 condensation has been suggested to support formation of the pericentriolar material
483 surrounding centrosomes (Feng et al., 2017; Jiang et al., 2021; Woodruff et al., 2017;
484 Zwicker et al., 2014). Last, the ability of the Pcp1-dependent diffusion barrier to form over
485 holes that span from tens to hundreds of nanometers in diameter (Figure 3) suggests a
486 remarkable plasticity in the nature of the barrier that could be consistent with an
487 unstructured biomolecular condensate. Future work will be needed to explore the
488 physiochemical properties of this barrier more fully, and in particular how its scale can be
489 modulated.

490 The Pcp1 barrier is sensitive to ESCRT perturbation presumably because larger
491 holes put greater reliance on this proteinaceous plug. Building on this, we propose that
492 ESCRTs act as a molecular grommet that restricts the size of the NE hole during
493 anaphase B to a scale that can be effectively supported by the diffusion barrier.
494 Superficially, this grommet model has similarities to the “O-ring seal” model that has been
495 suggested to reside at sites of reforming NE surrounding kinetochore-attached
496 microtubules in mammalian cells (von Appen et al., 2020). The concept of an O-ring is
497 primarily based on the formation of a ring-shaped CHMP7-LEM2 co-polymer that is
498 observed surrounding microtubules *in vitro* (von Appen et al., 2020)—the structure formed
499 *in vivo* remains unknown. However, our quantitative analysis reveals that only ~16
500 molecules of Cmp7 reside at the NE hole in anaphase B (Table 1 and Supplementary

501 Figure S2), far less than would be necessary to line the 50–150 nm NE hole
502 (corresponding to the widths measured when Cmp7 is recruited to the SPB extrusion site;
503 Figure 3) if it forms a co-polymer analogous to that suggested for the mammalian CHMP7-
504 LEM2 (von Appen et al., 2020). We suggest that the grommet model outlined here is
505 distinct, favoring instead the possibility that Cmp7 (the sequence of which contains
506 elements of both ESCRT-II and ESCRT-III family members) is a seed filament for the
507 assembly of additional downstream ESCRTs, akin to models that suggest a sequential
508 assembly order of ESCRT-IIIs at endosomes (Babst et al., 2002; Henne et al., 2012;
509 Pfitzner et al., 2020; Saksena et al., 2009; Teis et al., 2008) as well as other contexts that
510 begin with ESCRT-I and ESCRT-II proteins (Vietri et al., 2020). Such a model predicts
511 that Cmp7 is required for all ESCRT recruitment to the NE, which is indeed the case
512 (Figure 2). As CHMP7 is also required for ESCRT subunit recruitment to the NE in
513 mammalian cells at mitotic exit (Gu et al., 2017; Olmos et al., 2016), we suggest that the
514 fundamentals of ESCRT recruitment and function in *S. pombe* and mammalian cells are
515 highly similar. Subtleties between the two models will need to be revealed in future studies
516 that examine the copy number of ESCRTs at well-defined NE holes in mammalian cells
517 in the manner that we have performed here.
518 Although the observed copy number of Cmp7 molecules indicates that they may
519 not be able to independently line a 50–150 nm NE hole, they may nonetheless be
520 constituents of a more complex polymer that includes the Wave 2 ESCRTs, Vps32 and
521 Ist1, which are found at much higher copy numbers than Cmp7 (Table 1 and
522 Supplementary Figure S2). Indeed, based on the recruitment timing (Figure 1) and its
523 relationship to the normal constriction of the NE hole (Figure 3), we infer that a polymer(s)
524 consisting of Wave 1 and 2 ESCRTs comprises the grommet. This grommet appears to
525 restrict the NE hole diameter to support the Pcp1-dependent diffusion barrier (Figure 6).
526 However, as we observe that the NE hole shrinks from 150 nm to 50 nm during the Wave
527 1 and 2 recruitment period, it is also possible that the grommet is responsible for
528 physically driving its constriction. We speculate that this function could be attributed to
529 Ist1, which is thought to contribute to ILV neck constriction prior to membrane scission
530 during ILV formation (McCullough et al., 2015; Nguyen et al., 2020; Pfitzner et al., 2020),
531 with the caveat that the dimensions of a constricting ILV is an order of magnitude smaller

532 than the NE hole. This comparison further highlights a key difference between the order
533 of assembly/composition of ESCRTs at the NE compared to at endosomes, where Ist1 is
534 instead recruited much later than Vps32 (Pfitzner et al., 2020). Ultimately a model of
535 membrane fission at the NE must incorporate this difference, as well as the apparent
536 absence of the ESCRT-III Did2; we note, however, that the mammalian Did2 ortholog,
537 CHMP2A, was reported to localize to the reforming NE at mitotic exit, opening up the
538 alternative possibility that the levels of Did2-GFP present are below our threshold of
539 detection (Vietri et al., 2015) (Supplementary Figures S1A and S1B).

540 Our data clearly underscore that ESCRTs are required for the penultimate step of
541 NE sealing, likely through a membrane fission mechanism (Figure 3). However, our
542 observation of NE holes as small as 20 nm in the absence of Cmp7 suggests ESCRT-
543 independent mechanisms capable of minimizing the persistent NE hole in G_2, possibly
544 involving local lipid synthesis or flow of membrane from the ER (Kinugasa et al., 2019;
545 Kume et al., 2019; Penfield et al., 2020); normal nucleocytoplasmic compartmentalization
546 in this context further suggests the presence of a functional barrier to diffusion residing in
547 the persistent NE hole. Interestingly, our data also support that the NE sealing mechanism
548 requires maturation of the ESCRT filament including a wholesale replacement from a
549 Cmp7-Vps32-Ist1 grommet in late anaphase B to a NE sealing modality consisting of
550 Vps24 and Did4 in the subsequent G_1/S (Figures 2 and 4). Indeed, temporally the release
551 of Cmp7 occurs in concert with recruitment of the Wave 3 ESCRTs (Figure 1). Cmp7
552 therefore acts as a seed that initiates a sequence of ESCRT recruitment events, ultimately
553 leading to a mature state of a Wave 3 ESCRT filament that drives NE sealing. Disrupting
554 Wave 3 ESCRTs (Vps24 or Did4) drives the persistence of a Wave 1 state in which Cmp7
555 is found at an abnormally high copy number, apparently stuck in the NE hole that fails to
556 seal (Figures 2 and 4).

557 The observations that both disrupting ESCRT recruitment (*cmp7*Δ cells, Figure 3)
558 or accumulating a stalled ESCRT assembly (*did4*Δ cells, Figure 4) compromise NE
559 sealing has several implications for interpreting how loss of function of ESCRTs manifest
560 more generally. As nucleocytoplasmic compartmentalization can appear grossly normal
561 despite the persistence of these small NE holes, their presence may be undetected by
562 monitoring reporter proteins (Figure 5A). Thus, these observations highlight that it will be

563 important to revisit data suggesting ESCRT-independent NE sealing mechanisms that
564 did not include ultrastructural analysis. Perhaps most importantly, we think it likely that
565 persistent NE holes could lead to an unstable NE barrier that is more susceptible to further
566 perturbation. As loss of Cmp7 and persistent Cmp7 converge in precipitating a failure of
567 NE sealing, this work provides a useful framework to interpret the consequences of
568 ESCRT loss or gain of function in the context of disease. For example, variants in the
569 CHMP2B gene (ortholog of Did4) cause frontotemporal dementia (Skibinski et al., 2005)
570 and the aberrant nuclear entry of CHMP7 is upstream of a pathological cascade that could
571 contribute to both sporadic and familial forms of amyotrophic lateral sclerosis (Coyne et
572 al., 2021). In both scenarios, it is possible that improper clearance of CHMP7 could
573 compromise the integrity of the NE over timescales beyond that easily monitored in cell
574 culture. Further, it will be interesting to examine if some cancer cells are prone to repeated
575 nuclear ruptures due to NE nanoholes arising from inefficient ESCRT-mediated repair,
576 rendering them more fragile.
577

578 **ACKNOWLEDGEMENTS**

579 We thank the Center for Cellular and Molecular Imaging, Electron Microscopy Facility at
580 Yale School of Medicine for assistance with EM, particularly Morven Graham and Xinran
581 Liu. Additionally, we thank Elisa Rodriguez for technical support, and Li-Lin Du for yeast
582 strains. This work was supported by the National Institutes of Health (R01 GM105672 to
583 C.P. Lusk; F32 GM139285 to N.R. Ader) and an Allen Distinguished Investigator Award,
584 a Paul G. Allen Frontiers Group advised grant of the Paul G. Allen Family Foundation
585 (M.C. King).

586

587 **METHODS**

588 ***S. pombe* culture and strain generation.** Strains used in this study are listed in
589 Supplemental Table S2. Strains were cultured and mated using standard procedures and
590 media (Moreno et al., 1991). In brief, *S. pombe* were cultured on yeast extract
591 supplemented with 250 mg/liter adenine, histidine, leucine, uracil, and lysine
592 hydrochloride (YE5S) agar plates and liquid cultures. For experiments with MGM4, cells
593 were grown in Edinburgh minimal medium supplemented with 250 mg/liter adenine,
594 histidine, leucine, uracil, and lysine hydrochloride (EMM5S) overnight prior to imaging. C-
595 terminal tagging and gene replacement (knockout) were performed using the pFA6a,
596 MX6-based drug resistance cassettes (Bahler et al., 1998; Hentges et al., 2005) using *S.*
597 *pombe* genome information available through PomBase (Harris et al., 2022; Wood et al.,
598 2002). Visualization and virtual manipulation of DNA sequences was facilitated by using
599 ApE 2.0.61 (Davis and Jorgensen, 2022). For all GFP fusions, mEGFP was used. For C-
600 terminal tagging of Cmp7 for AID depletion we used pDB4581, a gift from Li-Lin Du
601 (Addgene plasmid # 171124) (Zhang et al., 2022). All genomic integrations were
602 confirmed by screening of individual clones by PCR of whole yeast (colony PCR) (Huxley
603 et al., 1990) with primers designed to amplify only a genomic insertion at the targeted
604 locus following a standard lithium acetate transformation procedure (Murray et al., 2016).

605 As has been previously shown, dysfunctional tagged ESCRT proteins display a
606 loss of dynamic remodeling and aberrantly accumulate in class E endosomes (Teis et al.,
607 2008). Thus, to generate functional GFP-ESCRTs, we first attempted C-terminal tagging
608 using a 3×HA linker. For Cmp7-3×HA-GFP, Ist1-3×HA-GFP, and Did2-3×HA-GFP this
609 strategy yielded GFP-ESCRTs which were dynamic by live-cell imaging (Figure 1) and
610 capable of generating progeny when mated. As we noted that expression of Vps32-3×HA-
611 GFP and Did4-3×HA-GFP appeared to drive a dominant negative phenotype that
612 inhibited tetrad formation, we used an N-terminal tagging strategy for tagging of Vps32,
613 Did4, and Vps24. N-terminal GFP-tagging of Vps32, Vps24, and Did4 was performed by
614 inserting a pJK148 plasmid cut with NruI at the *leu1-32* locus in a strain with the
615 endogenous gene knocked out (pNA32 for GFP-3×HA-Vsp32, pNA23 for GFP-3×HA-
616 Vps32, and pNA45 for GFP-3×HA-Did4; see Supplementary Table S2 for full plasmid list)
617 (Keeney and Boeke, 1994). To generate pNA22, pNA23, and pNA45 plasmids, we

618 performed Gibson Assembly of the following sequences: (1) promoter (500 bp upstream
619 of start 5' UTR) + 5'UTR, (2) GFP-3×HA, (3) open reading frame + 3'UTR + terminator
620 (500 bp downstream of stop codon) (Gibson et al., 2009). Strains with GFP-3×HA -Vps32,
621 GFP-3×HA -Vps24, and GFP-3×HA -Did4 had dynamic GFP-ESCRT foci (Figure 1) and
622 had no apparent defect in mating, producing viable tetrads.
623
624 **Live-cell fluorescence microscopy.** Cells expressing fluorescent protein fusions were
625 grown to log phase (OD_{600} 0.4–0.8) in YE5S supplemented with an additional 250 mg/L
626 adenine (to ensure low autofluorescence) and 0.1 mM *n*-propyl gallate (NPG) (an oxygen
627 scavenger to reduce photobleaching and mitochondrial autofluorescence), concentrated
628 by 20 s centrifugation at 2000× *g*, sandwiched between a #1.5 glass coverslip (VWR
629 48393) and a glass slide (Thermo Fischer Scientific 420), and sealed with VALAP (1:1:1,
630 vaseline:lanonin:paraffin). Image acquisition was performed on a DeltaVision microscope
631 (Applied Precision; GE Healthcare) using Resolve3D in SoftWoRx using the Insight SSI
632 4-color Live Cell filter set (ex425–495/em500–550 nm for GFP, ex555–590/em600–675
633 nm for mCherry) on a CoolSNAP HQ^2 CCD (Photometrics) or Evolve-512 EMMCD
634 (Photometrics) with either an UPlanSapo 100× 1.4 NA oil immersion objective (Olympus)
635 or a PlanApo 63× 1.42 NA oil immersion objective (Olympus) and an AURA light engine
636 (Lumencor) at 32% transmission or 100% transmission for up to 1 s. Cells were imaged
637 over 4.8–5 µm in the z-plane at 0.2 intervals for counting, 0.5 µm for compartmentalization
638 (MGM4 and MGM2), and 0.2–0.4 µm for all other experiments. Deconvolution was
639 performed using SoftWoRx. For timelapse experiments with drug delivery, cells were first
640 loaded into a CellASIC ONIX microfluidic plate (Millipore Y04C) before imaging.
641 Microfluidics were controlled by the CellASIC ONIX microfluidic platform (Millipore EV262,
642 MIC230, GM230). For Cmp7-AID depletion, 5IAA (TCI Chemicals, A3390) was dissolved
643 in DMSO to make a 1 mM stock solution and used at a final concentration of 100 nM in
644 culture. For treatment with 1,6-HD, 1,6-hexanediol (Alfa Aesar, A12439) was dissolved in
645 YE5S plus 250 mg/L adenine to make a 25% stock solution, which was diluted to either
646 2.5% or 5% as needed. Fluorescence micrographs were viewed and analyzed using Fiji
647 2.3.0/1.53q unless otherwise noted (Schindelin et al., 2012).
648

649 **Image Display**. All representative micrographs are displayed to maximize the displayed
650 dynamic range without pixel saturation in the linear range. When mCherry-Atb2 and Pcp1-
651 mCherry or mCherry-Atb2 and Sad1-mCherry are displayed together, the gamma has
652 been adjusted to 0.05 to allow both fluorophores to be displayed without pixel saturation.
653 All magnified ROIs of fluorescence micrographs were independently adjusted.
654
655 **Cell cycle classification for GFP-ESCRT localization to SPB extrusion site.** To
656 classify cells into phases of the cell cycle from still images, we used the following criteria:
657 Cells with mitotic spindles longer than 3 μm were considered to be in anaphase B and
658 were converted to time in anaphase B using the following formula:

659 $$\text{Time in anaphase B} = \frac{\text{spindle length (μm)}}{0.70\ \text{μm min}^{-1}} - 4.29\ \text{min}$$

660 We used the rate of spindle elongation of 0.7 μm/min in anaphase B as determined in
661 (Krüger et al., 2019) and the correction factor of 4.29 min represents a spindle length of
662 3 μm at the anaphase A/B transition. Cells with mitotic spindles longer than 3 μm, but
663 smaller than 6.35 μm were classified as early anaphase B (approximately 0–5 min into
664 anaphase B). Cells with spindles between 6.35 μm and 8.39 μm were classified as mid
665 anaphase B (approximately 5–7.5 min into anaphase B) and any cell with a spindle longer
666 than 8.39 μm was classified as late anaphase B (>7.5 min into anaphase B). Late G_1/S
667 cells were distinguished from early G_1/S cells by the lack of microtubules spanning the
668 septum region. For each phase of the cell cycle the percentage of SPB foci (Sad1-
669 mCherry or Pcp1-mCherry) that colocalized with the GFP-ESCRT was quantified for still
670 images as shown in Figures 1C, 2C–E, 2G, and 2I as well as Supplementary Figures S1B
671 and S3C. Quantification was performed across three biological replicates with at least 50
672 nuclei per replicate.
673
674 **Assessing the timing of GFP-ESCRT at SPB in anaphase B.** Strains expressing a
675 GFP-ESCRT protein, a SPB marker (Sad1-mCherry or Pcp1-mCherry), and mCherry-
676 Atb2 were imaged every 3 min for approximately 20 min. For cells entering anaphase B,
677 we recorded the length of the mitotic spindle in the first frame of the time-series where a
678 focus of the GFP-ESCRT could be discerned. These spindle lengths were converted to

679 time in anaphase B using the above formula (Figure 1D). We also used this method to
680 quantify the timing of SPB extrusion and NE constriction (Figure 1D, vertical gray bars).
681 Quantification was performed across three biological replicates with at least 50 nuclei per
682 replicate.
683
684 **Quantification of average copy number of ESCRT-III subunits.** Cells were prepared
685 for imaging by overnight culture in YE5S plus 250 mg/L adenine + 0.1 mM NPG to log
686 phase. Cells (MKSP3186) expressing Fta3-GFP were mounted on the same pad as a
687 GFP-ESCRT-expressing strain of interest. Cells were imaged as above. Images were
688 then analyzed using a custom MATLAB script, 'Find_n_Fit_Spots'
689 (https://github.com/LusKingLab/Find_n_Fit_Spots_3D). First, spots were detected using
690 'findIrregularSpots3', a custom-written MATLAB code that finds fluorescent objects
691 regardless of their shape. Briefly, the code identifies all the brightest pixels within sub-
692 volumes of a given size. Then, it calculates the ratio of the mean intensities of "central"
693 pixels over "edge" pixels. If the ratio is above a given threshold, the code keeps the
694 identified spot and calculates its 3D coordinates as an intensity-weighted centroid of
695 pixels. Second, for each "good" spot, x-y-coordinates were used to crop a circular image
696 with R = 7 pixels around the spot from the best 2D image (determined by z-coordinate)
697 which was fitted by the linear combination of a 2D Gaussian and error function, *erf*, to
698 account for nuclear edge background signal. The volume of the best Gaussian fit was
699 then used as a spot intensity. Identified spots were then manually curated to classify the
700 spot (Fta3-GFP or GFP-ESCRT) based on secondary fluorescent markers. Position in
701 the cell cycle was determined using brightfield images and, for GFP-ESCRT strains,
702 mCherry-Atb2. For each GFP-ESCRT focus, the copy number was determined by
703 dividing the intensity of the focus by the average intensity of mitotic Fta3-GFP, previously
704 calculated to be approximately 111 molecules (Lawrimore et al., 2011). For the
705 comparison of Fta3-GFP intensities across cell cycles (Supplemental Figures S2E–S2G),
706 the measured intensity is plotted by position in the cell cycle. To allow comparisons across
707 three biological replicates, individual datapoints were normalized to the average value for
708 each cell cycle position within the replicate. Fta3-GFP or GFP-ESCRT foci identified as
709 outliers using ROUT test Q = 1%, 1 iteration were excluded.

710

711 **Quantification of N/C ratio of fluorescent reporters.** To calculate the ratio of MGM4
712 and MGM2 fluorescent reporters in the in nucleoplasm vs. cytoplasm, we measured the
713 mean intensity of regions within the nucleoplasm, cytoplasm (avoiding vacuoles), and
714 outside of the cells (background). The background mean intensity was subtracted from
715 both the nucleoplasm and cytoplasmic mean intensities before calculating the N/C ratio.
716 The individual N/C ratios were then binned with 0.05 bin size using Microsoft Excel. We
717 displayed these data as a histogram, where the percentage of nuclei in each bin is shown.
718 For percentage change of N/C ratio in time-series imaging, the N/C ratio of the first frame
719 of the movie was subtracted from the N/C ratio of the last frame and then divided by the
720 N/C ratio of the first frame. Quantification was performed across three biological replicates
721 with at least 50 cells per replicate.
722

723 **Quantification of MGM4 nuclear fluorescence over time**. To analyze the fluorescence
724 intensity of nuclear MGM4 reporter, we first corrected for photobleaching using the
725 "Bleach Correction" function in Fiji with an exponential fit. For each cell, we measured the
726 mean fluorescence intensity of a region within the nucleoplasm for each frame of a time
727 series. To compare cells within and across populations, background subtracted intensity
728 measurements were normalized to the intensity of the nuclear region in the first frame.
729 Quantification was performed across three biological replicates with at least 5 nuclei per
730 replicate.
731

732 **Quantification of Cmp7-GFP fluorescence intensity in *did4*Δ cells**. To compare the
733 intensity of Cmp7-GFP at the SPB site across the cell cycle, we measured the mean
734 intensity the GFP channel in a background-subtracted circular area. Position in the cell
735 cycle was determined by mCherry-Atb2 morphology. To allow comparisons across three
736 biological replicates, individual datapoints were normalized to the average value for
737 mitotic cells with visible Cmp7-GFP foci. At least 30 cells were analyzed in each of three
738 biological replicates.
739

740 **Correlative light and electron microscopy.** CLEM of resin-embedded cells was
741 performed as described by Kukulski et al. (2012). In brief, cells were grown overnight in
742 YE5S plus 250 mg/L adenine to log phase before being concentrated onto a 0.45 µm
743 nitrocellulose membrane (Millipore HAWP02500) using a microanalysis filter setup
744 (Millipore XX1012500). Concentrated cells were transferred using either a blunted
745 toothpick or micropipette to the 200-µm recess of an aluminum platelet (Engineering
746 Office M. Wohlwend 241) (McDonald, 1999). Platelets were then frozen using a high-
747 pressure freezer (Leica Microsystems HPM100). Samples were freeze substituted in 0.1–
748 5% uranyl acetate in acetone and embedded in Lowicryl HM20 (Polysciences) with
749 automated temperature control (Leica Microsystems EM-AFS2), manual agitation and
750 solution exchange. Resin-embedded cells were sectioned to a 250 nm nominal thickness
751 using an ultramicrotome (Leica Artos 3D) equipped with a diamond knife (Diatome) before
752 being collected on 200 mesh copper grids with carbon support (Ted Pella 01840).
753 Fluorescence micrographs of grids were acquired using a DeltaVision microscope
754 with the optical configuration as described above for live-cell imaging. For each grid
755 square of interest, 10 z-sections were acquired every 250 nm with 3 s exposure with GFP
756 and mCherry imaging setup at 32% transmission. 15 nm protein A-coated gold beads
757 (Cell Microscopy Core, University Medical Center Utrecht) were adhered to grids prior to
758 EM to aid in tilt-series alignment prior to tomogram reconstruction.
759 Single or dual-axis tilt series were collected on an electron microscope (FEI TF20)
760 operated at 200 kV using a high-tilt tomography holder (Fischione Instruments 2020) from
761 approximately -60 to +60 degrees (one-degree increments) at a binned pixel size of 1.242
762 nm on a 4k × 4k Eagle CCD (FEI) using a 150 µm C2 aperture and a 100 µm objective
763 aperture in an automated fashion using SerialEM (Mastronarde, 2005). Reconstruction
764 and segmentation were performed using IMOD (Kremer et al., 1996), with the former in
765 an automated fashion (Mastronarde and Held, 2017). For better visibility in shown virtual
766 slices, a nonlinear anisotropic diffusion and Gaussian filter were applied in IMOD.
767 Fluorescence micrographs have been rotated to match the orientation of virtual slices and
768 adjusted for contrast individually.
769

770 **Measurement of NE hole width**. To measure the size of the NE hole at the SPB
771 extrusion site, we recorded the maximum 2D distance between the two pore membrane
772 regions of the NE abutting the SPB through the tomogram in IMOD. As some tomograms
773 captured only part of the NE in the visualized slice, some of these values may be
774 underestimates of the actual hole size (Figure 3I, open circles).
775
776 **Preparation of whole cell protein extracts and immunoblotting.** Overnight cultures of
777 yeast were grown in EMM5S to log phase. Cultures were centrifuged at 2000× *g* for 5 min
778 and cell pellets were washed with 1 mM EDTA. Cells were then pelleted and lysed in 2M
779 NaOH incubated for 10 min on ice. An equal volume of 50% trichloroacetic acid (TCA)
780 was mixed in before incubating for 10 min on ice and collecting the protein precipitate by
781 centrifugation. The pellet was then washed with –20˚C acetone and air-dried for 15 min.
782 The pellet was then dissolved in 5% SDS followed by an equal volume of SDS-PAGE
783 sample buffer containing urea (24 mM Tris-Cl pH 6.8, 9 M urea, 1 mM EDTA, 1% SDS,
784 10% glycerol). Samples were then shaken at 37˚C for 15 min before being centrifuged at
785 14,000× *g* for 15 min. Approximately equal loads of extracted protein was then resolved
786 on tris-glycine 10% SDS-PAGE gels and transferred using wet transfer to 0.2 µm
787 nitrocellulose membrane (Bio-Rad 1620112). Transferred proteins were then stained with
788 Ponceau S Solution (Sigma-Aldrich P3504) before being scanned on a flatbed scanner
789 (Epson V800 Photo). Blots were blocked overnight in blocking buffer (5% (w/v) dry
790 milk/TBST) and incubated with primary mouse α-mAID antibody (MBL M214-3) (diluted
791 1:1000 in blocking buffer). The blots were then incubated for 1 h at room temperature with
792 secondary HRP-conjugated goat anti-mouse antibodies (Invitrogen 3430). Antibody-
793 labeled proteins were visualized using SuperSignal West Femto Maximum Sensitivity
794 ECL Substrate (Thermo Fischer Scientific 34094) on a VersaDoc Imaging System (Bio-
795 Rad 4000 MP) with a 1.4 mm aperture and a three-minute exposure time. Digital images
796 of blots were processed using the “Despeckle” function in Fiji and then adjusted to
797 maximize intensity range without over- or under-saturation.
798
799 **Plate-based growth assays.** To evaluate relative colony growth rates, cells were grown
800 overnight in YE5S media. Cells were then diluted to 1 OD_{600} equivalent in YE5S before

801 sequentially plating 5 serial 1:10 dilutions on YE5S plates. The plates were incubated at
802 the indicated temperatures in figures/figure legends and scanned daily on a flatbed
803 scanner (Epson V800 Photo).
804
805 **Statistical methods**. All graphs were generated and analyzed for statistical significance
806 using Prism 9 (GraphPad). Tests used for each figure panel are denoted in figure legends.
807

808 **SUPPLEMENTARY FIGURES**

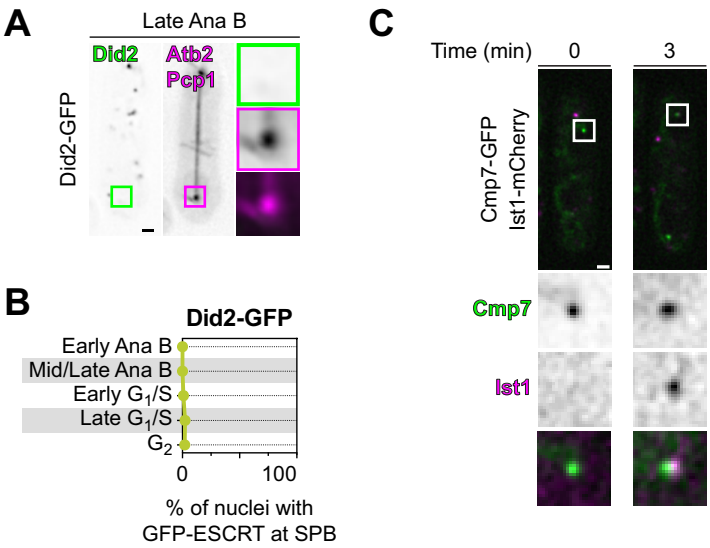

809

Supplementary Figure S1. Did2 is not detected at the SPB extrusion site, while Ist1 is recruited after Cmp7

A: Deconvolved fluorescence micrographs of Did2-GFP, mCherry-Atb2, and Pcp1-mCherry in a representative cell in anaphase B. Image of the Cmp7-GFP is on left, sum projection (over 4.8 µm) of mCherry-Atb2 in middle and magnifications of square ROI shown vertically arranged at right with (top to bottom) green, magenta and merged channels. Fluorescence intensity of magnified ROIs were independently adjusted in linear range. Scale bar, 1 µm. Magnified ROIs, 1.6 µm wide. To maximize image clarity, fluorescence intensity of magnified ROIs were independently adjusted in the linear range with the exception of the magenta channel where the gamma was adjusted to 0.05 to allow visualization of mCherry-Atb2 and Pcp1-mCherry without saturation.

B: Plot of the percentage of nuclei with Did2-GFP (MKSP3342) colocalized with SPB marker at indicated phases of the cell cycle. Points and error bars represent mean and range, respectively, across at least three biological replicates with at least 50 nuclei/GFP-ESCRT/replicate, N = 372 nuclei.

C: Deconvolved, time-lapse fluorescence microscopy of Cmp7-GFP (green) and Ist1-mCherry (magenta) in a late anaphase B cell (MKSP3521). Cell representative of population from two biological replicates. White boxes in overview micrographs indicate ROI magnified below images as single channel and composite images.

810

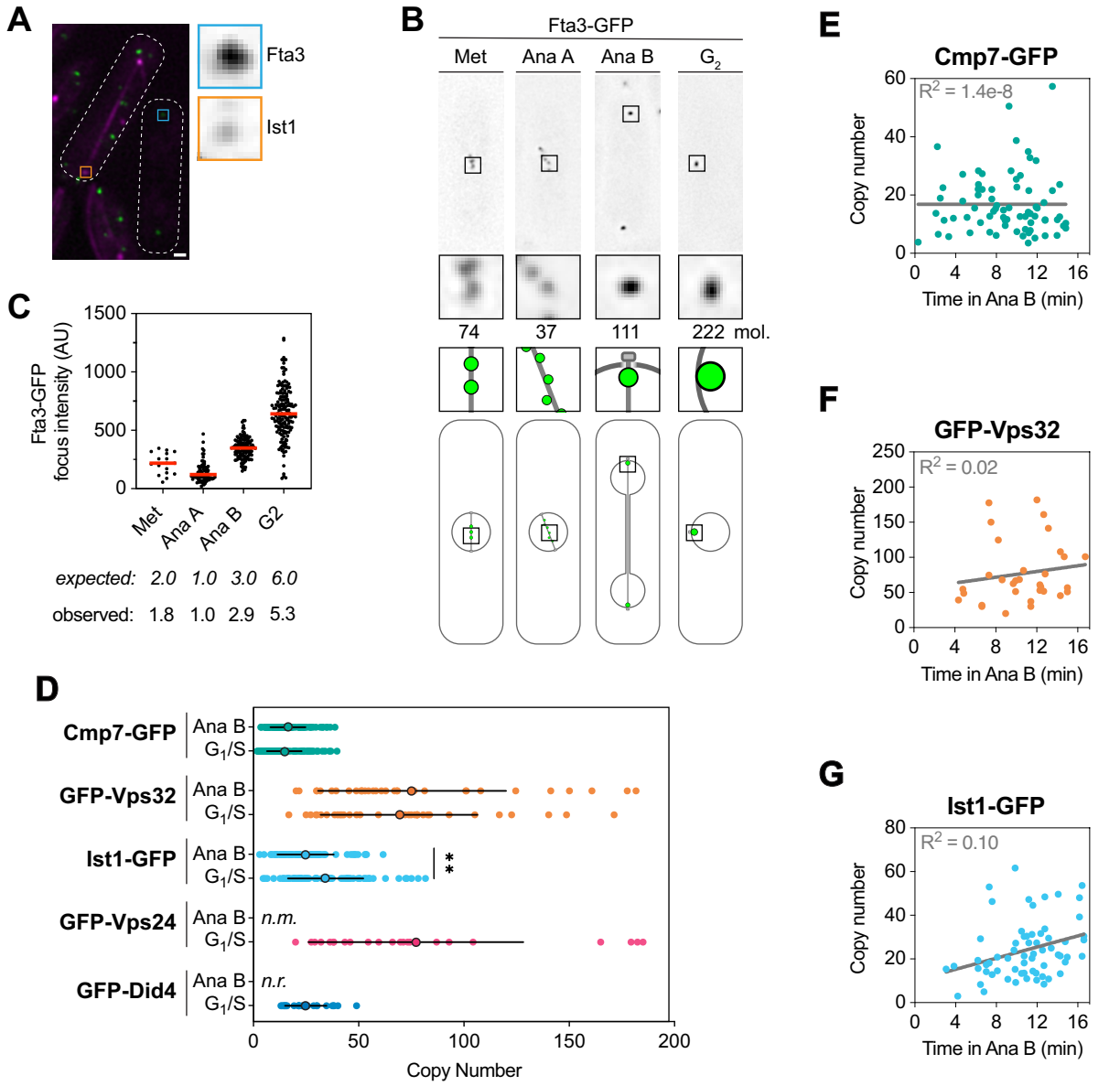

Supplementary Figure S2. Average copy number of ESCRTs at the SPB extrusion site determined by ratiometric quantification.

Figure legend continued on next page.

Supplementary Figure S2. Average copy number of ESCRTs at the SPB extrusion site determined by ratiometric quantification.

A: Deconvolved fluorescence micrographs of representative mixture of a GFP-ESCRT strain (Ist1-GFP, MKSP3365) and one expressing Fta3-GFP (MKSP3186). In top left, strain expressing Ist1-GFP (green), mCherry-Atb2 (magenta), and Sad1-mCherry (magenta). In bottom right, Fta3-GFP strain (green). Scale bar, 1 µm. Blue and orange boxes in overview micrographs indicate ROI magnified to the right of image as single channel images for Fta3-GFP and Ist1-GFP, respectively.

B: Deconvolved fluorescence micrographs of representative Fta3-GFP expressing cells (MKSP3186) at indicated cell cycle stage (top). Black boxes in overview micrographs indicate ROI magnified below images (middle). Schematic representation of Fta3-GFP appearance by cell cycle show (bottom). Number of molecules based on Lawrimore et al. (2011).

C: Scatter plot of Fta3-GFP focus fluorescence intensity at indicated cell cycle stages in MKSP3186. Red lines represent the median. Expected and observed ratios of Fta3 molecules shown below. N = 366 foci across three biological replicates with at least 50 foci/replicate.

D: Number of molecules of indicated GFP-ESCRT at the SPB extrusion site during all phases of the cell cycle. Outlined point and black lines represent mean and standard deviation, respectively. *n.r.*, not recruited. *n.m.*, not measured. Data was collected over at least three biological replicates. Kruskal-Wallis test performed across all cell cycle phases for each ESCRT individually with Dunn's multiple comparisons across all other cell cycle phases (*, $p < 0.05$; **, $p<0.01$; all others, $p \geq 0.05$). Fta3-GFP (MKSP3186); Cmp7-GFP (MKSP3363), N = 196 foci; GFP-Vps32 (MKSP3353), N = 68 foci; Ist1-GFP (MKSP3365), N = 147 foci; GFP-Vps24 (MKSP3352), N = 24 foci; GFP-Did4 (MKSP3334), N = 26 foci.

E–G: Copy number of indicated GFP-ESCRT shown as a function of time in anaphase B. Gray lines represent a simple linear regression with the R^2 shown in gray. Fta3-GFP (MKSP3186); Cmp7-GFP (MKSP3363), N = 73 foci; GFP-Vps32 (MKSP3353), N = 32 foci; Ist1-GFP (MKSP3365), N = 64 foci.

813

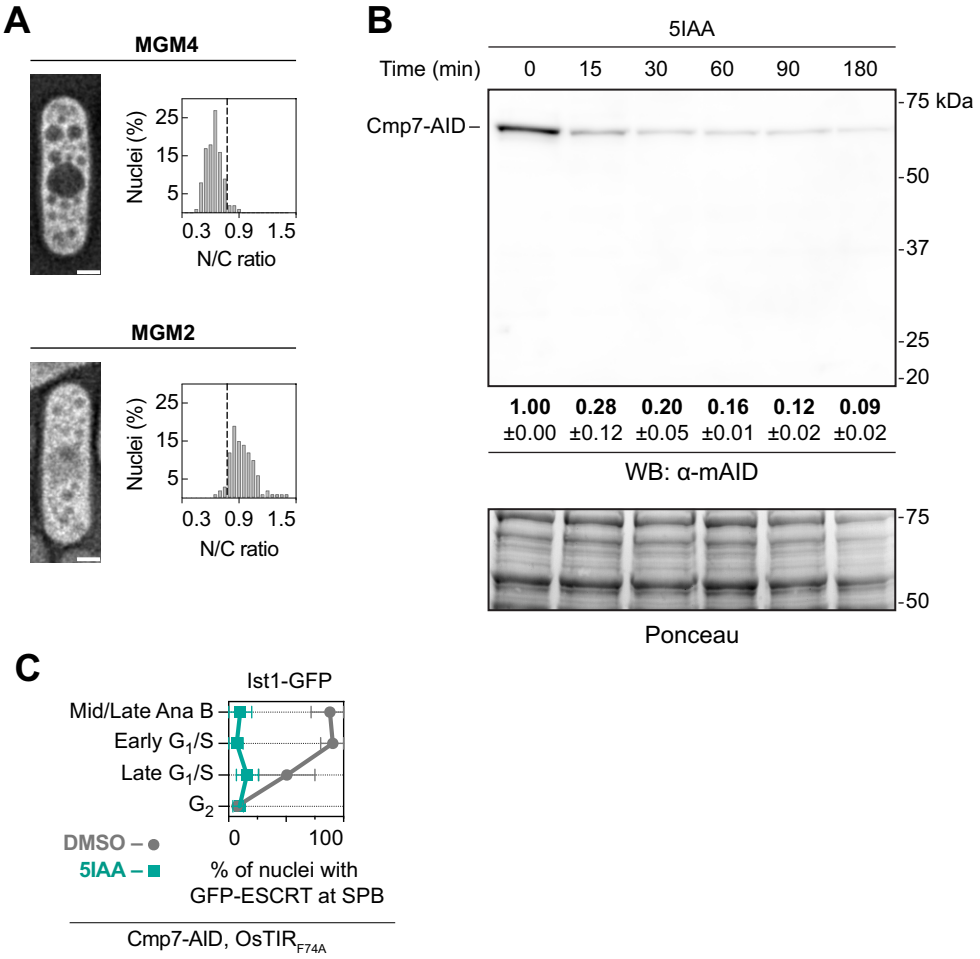

814

Supplementary Figure S3. MGM4 and MGM2 reporters; auxin induced degron (AID) system allows for fast degradation of Cmp7.

A: Deconvolved live-cell fluorescence microscopy of MGM4 (top left, MKSP3345) and MGM2 (bottom left, MKSP3501). Histogram of nucleoplasmic to cytoplasmic GFP fluorescence (N/C ratio) for individual cells shown to the right of each reporter. MGM4 data replotted from Figure 5A. Size between bins, 0.05. Dotted line at 0.75 bin. Quantification was performed for three biological replicates. MGM2, N = 177 nuclei, with at least 46 nuclei/biological replicate.

B: Representative western blot (WB) of Cmp7-AID levels (detected with an α-AID antibody) in total protein extracts from cells grown in the presence of 5IAA for the indicated times. Ponceau stain is shown at bottom to assess relative total protein loads. Relative amount of Cmp7-AID protein, normalized to T_0, is shown below WB as mean and standard deviation for three biological replicates.

C: Plots of the percentage of nuclei with Ist1-GFP colocalized with SPB marker at indicated phases of the cell cycle in cells (MKSP3625) expressing Cmp7-AID and $OsTIR1_{F74A}$. Cells were treated with DMSO (gray) or 5IAA (green) for 1 h. Points and error bars represent mean and range, respectively, across at least three biological replicates with at least 50 nuclei/GFP-ESCRT/replicate. DMSO, N = 273 nuclei; 5IAA, N = 296 nuclei.

815

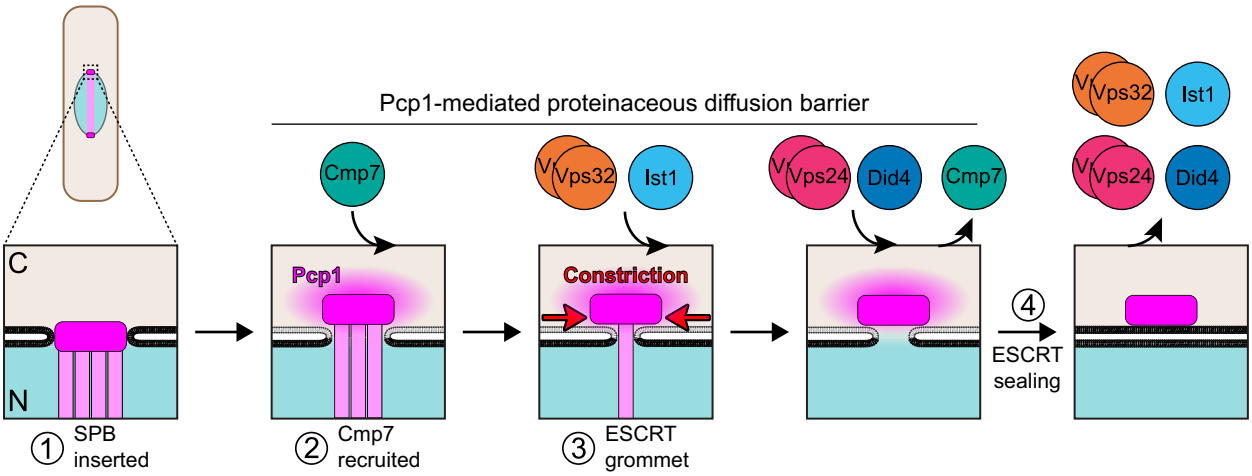

816

Supplementary Figure S4. An ESCRT grommet and Pcp1-dependent diffusion barrier maintain nuclear integrity

A model of NE sealing and maintenance of mitotic nuclear integrity by the ESCRT machinery and Pcp1. (1) In early mitosis, the SPB is inserted into the NE. (2) Once the SPB is extruded to the cytosol, Cmp7 is recruited by Heh1/Lem2 (not shown). Concurrently, Pcp1 contributes to the formation of a proteinaceous diffusion barrier sensitive to 2.5% 1,6-HD to prevent free diffusion through the unsealed NE. (3) A second wave of ESCRT recruitment comprising Vps32 and Ist1 occurs in late anaphase B, which generates a "grommet" that restricts the size of the NE hole and supports the Pcp1-diffusion barrier. (4) Finally, in the G_1/S of the following cell cycle, the third wave of ESCRTs, Did4 and Vps24, is recruited, displacing Cmp7 and sealing the NE.

817 **MOVIES**

Movie 1. CLEM and ET of a WT cell in early anaphase B. Electron tomogram of an early anaphase B cell (MKSP3180) with segmentation. NE, blue; SPB, dark orange; microtubules, yellow. Scale bar, 100 nm.

Movie 2. CLEM and ET of a WT cell in late anaphase B. Electron tomogram of a late anaphase B cell (MKSP3180) with segmentation. NE, blue; SPB, dark orange; microtubules, yellow. Annotations at end of movie show NPC and SPB extrusion hole. Scale bar, 100 nm.

Movie 3. CLEM and ET of a *cmp7*Δ cell in early anaphase B. Electron tomogram of an early anaphase B cell (MKSP3243) with segmentation. NE, blue; SPB, dark orange; microtubules, yellow. Scale bar, 100 nm.

Movie 4. CLEM and ET of a *cmp7*Δ cell in late anaphase B. Electron tomogram of a late anaphase B cell (MKSP3243) with segmentation. NE, blue; SPB, dark orange; microtubules, yellow. Scale bar, 100 nm.

818

819 **SUPPLEMENTARY TABLES**

Supplementary Table 1. GFP-tagging of key ESCRT machinery. ESCRT protein in *S. pombe* is shown on left. Orthologs in *S. cerevisiae* and *H. sapiens* are shown in center. Tagging approach to ensure function is shown on right.

Supplementary Table 2. List of *S. pombe* strains used in this study.

Supplementary Table 3. List of plasmids used in this study.

820 **REFERENCES**

821 Adell, M.A.Y., Migliano, S.M., Upadhyayula, S., Bykov, Y.S., Sprenger, S., Pakdel, M., Vogel, G.F., Jih, G.,
822 Skillern, W., Behrouzi, R., et al. (2017). Recruitment dynamics of ESCRT-III and Vps4 to endosomes and
823 implications for reverse membrane budding. Elife *6*, e31652. 10.7554/eLife.31652.

824 Babst, M., Katzmann, D.J., Estepa-Sabal, E.J., Meerloo, T., and Emr, S.D. (2002). ESCRT-III: an
825 endosome-associated heterooligomeric protein complex required for MVB sorting. Dev Cell *3*, 271-282.
826 10.1016/s1534-5807(02)00220-4.

827 Bahler, J., Wu, J.Q., Longtine, M.S., Shah, N.G., McKenzie, A., 3rd, Steever, A.B., Wach, A., Philippsen,
828 P., and Pringle, J.R. (1998). Heterologous modules for efficient and versatile PCR-based gene targeting in
829 *Schizosaccharomyces pombe*. Yeast *14*, 943-951. 10.1002/(SICI)1097-0061(199807)14:10<943::AID-
830 YEA292>3.0.CO;2-Y.

831 Byers, B., and Goetsch, L. (1975). Behavior of spindles and spindle plaques in the cell cycle and conjugation
832 of *Saccharomyces cerevisiae*. J Bacteriol *124*, 511-523. 10.1128/jb.124.1.511-523.1975.

833 Celetti, G., Paci, G., Caria, J., VanDelinder, V., Bachand, G., and Lemke, E.A. (2020). The liquid state of
834 FG-nucleoporins mimics permeability barrier properties of nuclear pore complexes. J Cell Biol *219*.
835 10.1083/jcb.201907157.

836 Chiu, Y.P., Sun, Y.C., Qiu, D.C., Lin, Y.H., Chen, Y.Q., Kuo, J.C., and Huang, J.R. (2020). Liquid-liquid
837 phase separation and extracellular multivalent interactions in the tale of galectin-3. Nat Commun *11*, 1229.
838 10.1038/s41467-020-15007-3.

839 Coyne, A.N., Baskerville, V., Zaepfel, B.L., Dickson, D.W., Rigo, F., Bennett, F., Lusk, C.P., and Rothstein,
840 J.D. (2021). Nuclear accumulation of CHMP7 initiates nuclear pore complex injury and subsequent TDP-
841 43 dysfunction in sporadic and familial ALS. Sci Transl Med *13*. 10.1126/scitranslmed.abe1923.

842 Davis, M.W., and Jorgensen, E.M. (2022). ApE, A Plasmid Editor: a freely available DNA manipulation and
843 visualization program. Front Bioinform *2*, 818619. 10.3389/fbinf.2022.818619.

844 Denais, C.M., Gilbert, R.M., Isermann, P., McGregor, A.L., te Lindert, M., Weigelin, B., Davidson, P.M.,
845 Friedl, P., Wolf, K., and Lammerding, J. (2016). Nuclear envelope rupture and repair during cancer cell
846 migration. Science *352*, 353-358. 10.1126/science.aad7297.

847 Dey, G., Culley, S., Curran, S., Schmidt, U., Henriques, R., Kukulski, W., and Baum, B. (2020). Closed
848 mitosis requires local disassembly of the nuclear envelope. Nature *585*, 119-123. 10.1038/s41586-020-
849 2648-3.

850 Ding, R., West, R.R., Morphew, D.M., Oakley, B.R., and McIntosh, J.R. (1997). The spindle pole body of
851 *Schizosaccharomyces pombe* enters and leaves the nuclear envelope as the cell cycle proceeds. Mol Biol
852 Cell *8*, 1461-1479. 10.1091/mbc.8.8.1461.

853 Dultz, E., Wojtynek, M., Medalia, O., and Onischenko, E. (2022). The nuclear pore complex: birth, life, and
854 death of a cellular behemoth. Cells *11*. 10.3390/cells11091456.

855 Feng, Z., Caballe, A., Wainman, A., Johnson, S., Haensele, A.F.M., Cottee, M.A., Conduit, P.T., Lea, S.M.,
856 and Raff, J.W. (2017). Structural basis for mitotic centrosome assembly in flies. Cell *169*, 1078-1089 e1013.
857 10.1016/j.cell.2017.05.030.

858 Fong, C.S., Sato, M., and Toda, T. (2010). Fission yeast Pcp1 links polo kinase-mediated mitotic entry to
859 gamma-tubulin-dependent spindle formation. EMBO J *29*, 120-130. 10.1038/emboj.2009.331.

860 Frey, S., Richter, R.P., and Görlich, D. (2006). FG-rich repeats of nuclear pore proteins form a three-
861 dimensional meshwork with hydrogel-like properties. Science *314*, 815-817. 10.1126/science.1132516.

862 Gibson, D.G., Young, L., Chuang, R.Y., Venter, J.C., Hutchison, C.A., 3rd, and Smith, H.O. (2009).
863 Enzymatic assembly of DNA molecules up to several hundred kilobases. Nat Methods *6*, 343-345.
864 10.1038/nmeth.1318.

865 Gu, M., LaJoie, D., Chen, O.S., von Appen, A., Ladinsky, M.S., Redd, M.J., Nikolova, L., Bjorkman, P.J.,
866 Sundquist, W.I., Ullman, K.S., and Frost, A. (2017). LEM2 recruits CHMP7 for ESCRT-mediated nuclear
867 envelope closure in fission yeast and human cells. Proc Natl Acad Sci U S A *114*, E2166-E2175.
868 10.1073/pnas.1613916114.

869 Halfmann, C.T., Sears, R.M., Katiyar, A., Busselman, B.W., Aman, L.K., Zhang, Q., O'Bryan, C.S., Angelini,
870 T.E., Lele, T.P., and Roux, K.J. (2019). Repair of nuclear ruptures requires barrier-to-autointegration factor.
871 J Cell Biol *218*, 2136-2149. 10.1083/jcb.201901116.

872 Harris, M.A., Rutherford, K.M., Hayles, J., Lock, A., Bahler, J., Oliver, S.G., Mata, J., and Wood, V. (2022).
873 Fission stories: using PomBase to understand *Schizosaccharomyces pombe* biology. Genetics *220*.
874 10.1093/genetics/iyab222.

875 Henne, W.M., Buchkovich, N.J., Zhao, Y., and Emr, S.D. (2012). The endosomal sorting complex ESCRT-
876 II mediates the assembly and architecture of ESCRT-III helices. Cell *151*, 356-371.
877 10.1016/j.cell.2012.08.039.

878 Hentges, P., Van Driessche, B., Tafforeau, L., Vandenhaute, J., and Carr, A.M. (2005). Three novel
879 antibiotic marker cassettes for gene disruption and marker switching in *Schizosaccharomyces pombe*.
880 Yeast *22*, 1013-1019. 10.1002/yea.1291.

881 Huxley, C., Green, E.D., and Dunham, I. (1990). Rapid assessment of *S. cerevisiae* mating type by PCR.
882 Trends Genet *6*, 236. 10.1016/0168-9525(90)90190-h.

883 Jia, J., Claude-Taupin, A., Gu, Y., Choi, S.W., Peters, R., Bissa, B., Mudd, M.H., Allers, L., Pallikkuth, S.,
884 Lidke, K.A., et al. (2020). Galectin-3 coordinates a cellular system for lysosomal repair and removal. Dev
885 Cell *52*, 69-87 e68. 10.1016/j.devcel.2019.10.025.

886 Jiang, X., Ho, D.B.T., Mahe, K., Mia, J., Sepulveda, G., Antkowiak, M., Jiang, L., Yamada, S., and Jao, L.E.
887 (2021). Condensation of pericentrin proteins in human cells illuminates phase separation in centrosome
888 assembly. J Cell Sci *134*. 10.1242/jcs.258897.

889 Kanke, M., Nishimura, K., Kanemaki, M., Kakimoto, T., Takahashi, T.S., Nakagawa, T., and Masukata, H.
890 (2011). Auxin-inducible protein depletion system in fission yeast. BMC Cell Biol *12*, 8. 10.1186/1471-2121-
891 12-8.

892 Keeney, J.B., and Boeke, J.D. (1994). Efficient targeted integration at leu1-32 and ura4-294 in
893 *Schizosaccharomyces pombe*. Genetics *136*, 849-856.

894 Kinugasa, Y., Hirano, Y., Sawai, M., Ohno, Y., Shindo, T., Asakawa, H., Chikashige, Y., Shibata, S., Kihara,
895 A., Haraguchi, T., and Hiraoka, Y. (2019). The very-long-chain fatty acid elongase Elo2 rescues lethal
896 defects associated with loss of the nuclear barrier function in fission yeast cells. J Cell Sci *132*, jcs229021.
897 10.1242/jcs.229021.

898 Kono, Y., Adam, S.A., Sato, Y., Reddy, K.L., Zheng, Y., Medalia, O., Goldman, R.D., Kimura, H., and Shimi,
899 T. (2022). Nucleoplasmic lamin C rapidly accumulates at sites of nuclear envelope rupture with BAF and
900 cGAS. J Cell Biol *221*, e202201024. 10.1083/jcb.202201024.

901 Kremer, J.R., Mastronarde, D.N., and McIntosh, J.R. (1996). Computer visualization of three-dimensional
902 image data using IMOD. J Struct Biol *116*, 71-76. 10.1006/jsbi.1996.0013.

903 Krüger, L.K., Sanchez, J.L., Paoletti, A., and Tran, P.T. (2019). Kinesin-6 regulates cell-size-dependent
904 spindle elongation velocity to keep mitosis duration constant in fission yeast. Elife *8*, e42182.
905 10.7554/eLife.42182.

906 Kukulski, W., Schorb, M., Welsch, S., Picco, A., Kaksonen, M., and Briggs, J.A. (2012). Precise, correlated
907 fluorescence microscopy and electron tomography of lowicryl sections using fluorescent fiducial markers.
908 Methods Cell Biol *111*, 235-257. 10.1016/B978-0-12-416026-2.00013-3.

909 Kume, K., Cantwell, H., Burrell, A., and Nurse, P. (2019). Nuclear membrane protein Lem2 regulates
910 nuclear size through membrane flow. Nat Commun *10*, 1871. 10.1038/s41467-019-09623-x.

911 Lawrimore, J., Bloom, K.S., and Salmon, E.D. (2011). Point centromeres contain more than a single
912 centromere-specific Cse4 (CENP-A) nucleosome. J Cell Biol *195*, 573-582. 10.1083/jcb.201106036.

913 Lee, I.J., Stokasimov, E., Dempsey, N., Varberg, J.M., Jacob, E., Jaspersen, S.L., and Pellman, D. (2020).
914 Factors promoting nuclear envelope assembly independent of the canonical ESCRT pathway. J Cell Biol
915 *219*. 10.1083/jcb.201908232.

916 Makarova, M., and Oliferenko, S. (2016). Mixing and matching nuclear envelope remodeling and spindle
917 assembly strategies in the evolution of mitosis. Curr Opin Cell Biol *41*, 43-50. 10.1016/j.ceb.2016.03.016.

918 Mastronarde, D.N. (2005). Automated electron microscope tomography using robust prediction of specimen
919 movements. J Struct Biol *152*, 36-51. 10.1016/j.jsb.2005.07.007.

920 Mastronarde, D.N., and Held, S.R. (2017). Automated tilt series alignment and tomographic reconstruction
921 in IMOD. J Struct Biol *197*, 102-113. 10.1016/j.jsb.2016.07.011.

922 McCullough, J., Clippinger, A.K., Talledge, N., Skowyra, M.L., Saunders, M.G., Naismith, T.V., Colf, L.A.,
923 Afonine, P., Arthur, C., Sundquist, W.I., et al. (2015). Structure and membrane remodeling activity of
924 ESCRT-III helical polymers. Science *350*, 1548-1551. 10.1126/science.aad8305.

925 McCullough, J., Frost, A., and Sundquist, W.I. (2018). Structures, functions, and dynamics of ESCRT-
926 III/Vps4 membrane remodeling and fission complexes. Annu Rev Cell Dev Biol *34*, 85-109.
927 10.1146/annurev-cellbio-100616-060600.

928 McDonald, K. (1999). High-pressure freezing for preservation of high resolution fine structure and
929 antigenicity for immunolabeling. Methods Mol Biol *117*, 77-97. 10.1385/1-59259-201-5:77.

930 Mierzwa, B.E., Chiaruttini, N., Redondo-Morata, L., von Filseck, J.M., Konig, J., Larios, J., Poser, I., Muller-
931 Reichert, T., Scheuring, S., Roux, A., and Gerlich, D.W. (2017). Dynamic subunit turnover in ESCRT-III
932 assemblies is regulated by Vps4 to mediate membrane remodelling during cytokinesis. Nat Cell Biol *19*,
933 787-798. 10.1038/ncb3559.

934 Moreno, S., Klar, A., and Nurse, P. (1991). Molecular genetic analysis of fission yeast
935 Schizosaccharomyces pombe. Methods Enzymol *194*, 795-823. 10.1016/0076-6879(91)94059-I.

936 Murray, J.M., Watson, A.T., and Carr, A.M. (2016). Transformation of *Schizosaccharomyces pombe*: lithium
937 acetate/dimethyl sulfoxide procedure. Cold Spring Harb Protoc *2016*, pdb prot090969.
938 10.1101/pdb.prot090969.

939 Nguyen, H.C., Talledge, N., McCullough, J., Sharma, A., Moss, F.R., 3rd, Iwasa, J.H., Vershinin, M.D.,
940 Sundquist, W.I., and Frost, A. (2020). Membrane constriction and thinning by sequential ESCRT-III
941 polymerization. Nat Struct Mol Biol *27*, 392-399. 10.1038/s41594-020-0404-x.

942 O'Toole, E.T., Winey, M., and McIntosh, J.R. (1999). High-voltage electron tomography of spindle pole
943 bodies and early mitotic spindles in the yeast *Saccharomyces cerevisiae*. Mol Biol Cell *10*, 2017-2031.
944 10.1091/mbc.10.6.2017.

945 Olmos, Y., Hodgson, L., Mantell, J., Verkade, P., and Carlton, J.G. (2015). ESCRT-III controls nuclear
946 envelope reformation. Nature *522*, 236-239. 10.1038/nature14503.

947 Olmos, Y., Perdrix-Rosell, A., and Carlton, J.G. (2016). Membrane binding by CHMP7 coordinates ESCRT-
948 III-dependent nuclear envelope reformation. Curr Biol *26*, 2635-2641. 10.1016/j.cub.2016.07.039.

949 Penfield, L., Shankar, R., Szentgyorgyi, E., Laffitte, A., Mauro, M.S., Audhya, A., Muller-Reichert, T., and
950 Bahmanyar, S. (2020). Regulated lipid synthesis and LEM2/CHMP7 jointly control nuclear envelope
951 closure. J Cell Biol *219*. 10.1083/jcb.201908179.

952 Petri, M., Frey, S., Menzel, A., Görlich, D., and Techert, S. (2012). Structural characterization of nanoscale
953 meshworks within a nucleoporin FG hydrogel. Biomacromolecules *13*, 1882-1889. 10.1021/bm300412q.

954 Pfitzner, A.K., Mercier, V., Jiang, X., Moser von Filseck, J., Baum, B., Saric, A., and Roux, A. (2020). An
955 ESCRT-III polymerization sequence drives membrane deformation and fission. Cell *182*, 1140-1155 e1118.
956 10.1016/j.cell.2020.07.021.

957 Pfitzner, A.K., Moser von Filseck, J., and Roux, A. (2021). Principles of membrane remodeling by dynamic
958 ESCRT-III polymers. Trends Cell Biol *31*, 856-868. 10.1016/j.tcb.2021.04.005.

959 Pieper, G.H., Sprenger, S., Teis, D., and Oliferenko, S. (2020). ESCRT-III/Vps4 controls heterochromatin-
960 nuclear envelope attachments. Dev Cell *53*, 27-41 e26. 10.1016/j.devcel.2020.01.028.

961 Popken, P., Ghavami, A., Onck, P.R., Poolman, B., and Veenhoff, L.M. (2015). Size-dependent leak of
962 soluble and membrane proteins through the yeast nuclear pore complex. Mol Biol Cell *26*, 1386-1394.
963 10.1091/mbc.E14-07-1175.

964 Raab, M., Gentili, M., de Belly, H., Thiam, H.R., Vargas, P., Jimenez, A.J., Lautenschlaeger, F., Voituriez,
965 R., Lennon-Dumenil, A.M., Manel, N., and Piel, M. (2016). ESCRT III repairs nuclear envelope ruptures
966 during cell migration to limit DNA damage and cell death. Science *352*, 359-362. 10.1126/science.aad7611.

967 Radulovic, M., Schink, K.O., Wenzel, E.M., Nahse, V., Bongiovanni, A., Lafont, F., and Stenmark, H. (2018).
968 ESCRT-mediated lysosome repair precedes lysophagy and promotes cell survival. EMBO J *37*.
969 10.15252/embj.201899753.

970 Remec Pavlin, M., and Hurley, J.H. (2020). The ESCRTs - converging on mechanism. J Cell Sci *133*,
971 jcs240333. 10.1242/jcs.240333.

972 Ribbeck, K., and Görlich, D. (2002). The permeability barrier of nuclear pore complexes appears to operate
973 via hydrophobic exclusion. EMBO J *21*, 2664-2671. 10.1093/emboj/21.11.2664.

974 Saksena, S., Wahlman, J., Teis, D., Johnson, A.E., and Emr, S.D. (2009). Functional reconstitution of
975 ESCRT-III assembly and disassembly. Cell *136*, 97-109. 10.1016/j.cell.2008.11.013.

976 Samwer, M., Schneider, M.W.G., Hoefler, R., Schmalhorst, P.S., Jude, J.G., Zuber, J., and Gerlich, D.W.
977 (2017). DNA cross-bridging shapes a single nucleus from a set of mitotic chromosomes. Cell *170*, 956-972
978 e923. 10.1016/j.cell.2017.07.038.

979 Schindelin, J., Arganda-Carreras, I., Frise, E., Kaynig, V., Longair, M., Pietzsch, T., Preibisch, S., Rueden,
980 C., Saalfeld, S., Schmid, B., et al. (2012). Fiji: an open-source platform for biological-image analysis. Nat
981 Methods *9*, 676-682. 10.1038/nmeth.2019.

982 Shulga, N., and Goldfarb, D.S. (2003). Binding dynamics of structural nucleoporins govern nuclear pore
983 complex permeability and may mediate channel gating. Mol Cell Biol *23*, 534-542. 10.1128/MCB.23.2.534-
984 542.2003.

985 Skibinski, G., Parkinson, N.J., Brown, J.M., Chakrabarti, L., Lloyd, S.L., Hummerich, H., Nielsen, J.E.,
986 Hodges, J.R., Spillantini, M.G., Thusgaard, T., et al. (2005). Mutations in the endosomal ESCRTIII-complex
987 subunit CHMP2B in frontotemporal dementia. Nat Genet *37*, 806-808. 10.1038/ng1609.

988 Skowyra, M.L., Schlesinger, P.H., Naismith, T.V., and Hanson, P.I. (2018). Triggered recruitment of ESCRT
989 machinery promotes endolysosomal repair. Science *360*, eaar5078. 10.1126/science.aar5078.

990 Sohrmann, M., Schmidt, S., Hagan, I., and Simanis, V. (1998). Asymmetric segregation on spindle poles
991 of the *Schizosaccharomyces pombe* septum-inducing protein kinase Cdc7p. Genes Dev *12*, 84-94.
992 10.1101/gad.12.1.84.

993 Teis, D., Saksena, S., and Emr, S.D. (2008). Ordered assembly of the ESCRT-III complex on endosomes
994 is required to sequester cargo during MVB formation. Dev Cell *15*, 578-589. 10.1016/j.devcel.2008.08.013.

995 Thaller, D.J., Allegretti, M., Borah, S., Ronchi, P., Beck, M., and Lusk, C.P. (2019). An ESCRT-LEM protein
996 surveillance system is poised to directly monitor the nuclear envelope and nuclear transport system. Elife
997 *8*, e45284. 10.7554/eLife.45284.

998 Thaller, D.J., Tong, D., Marklew, C.J., Ader, N.R., Mannino, P.J., Borah, S., King, M.C., Ciani, B., and Lusk,
999 C.P. (2021). Direct binding of ESCRT protein Chm7 to phosphatidic acid-rich membranes at nuclear
1000 envelope herniations. J Cell Biol *220*. 10.1083/jcb.202004222.

1001 Ungricht, R., and Kutay, U. (2017). Mechanisms and functions of nuclear envelope remodelling. Nat Rev
1002 Mol Cell Biol *18*, 229-245. 10.1038/nrm.2016.153.

1003 Ventimiglia, L.N., Cuesta-Geijo, M.A., Martinelli, N., Caballe, A., Macheboeuf, P., Miguet, N., Parnham,
1004 I.M., Olmos, Y., Carlton, J.G., Weissenhorn, W., and Martin-Serrano, J. (2018). CC2D1B coordinates
1005 ESCRT-III activity during the mitotic reformation of the nuclear envelope. Dev Cell *47*, 547-563 e546.
1006 10.1016/j.devcel.2018.11.012.

1007 Vietri, M., Radulovic, M., and Stenmark, H. (2020). The many functions of ESCRTs. Nat Rev Mol Cell Biol
1008 *21*, 25-42. 10.1038/s41580-019-0177-4.

1009 Vietri, M., Schink, K.O., Campsteijn, C., Wegner, C.S., Schultz, S.W., Christ, L., Thoresen, S.B., Brech, A.,
1010 Raiborg, C., and Stenmark, H. (2015). Spastin and ESCRT-III coordinate mitotic spindle disassembly and
1011 nuclear envelope sealing. Nature *522*, 231-235. 10.1038/nature14408.

1012 von Appen, A., LaJoie, D., Johnson, I.E., Trnka, M.J., Pick, S.M., Burlingame, A.L., Ullman, K.S., and Frost,
1013 A. (2020). LEM2 phase separation promotes ESCRT-mediated nuclear envelope reformation. Nature *582*,
1014 115-118. 10.1038/s41586-020-2232-x.

1015 Wälde, S., and King, M.C. (2014). The KASH protein Kms2 coordinates mitotic remodeling of the spindle
1016 pole body. J Cell Sci *127*, 3625-3640. 10.1242/jcs.154997.

1017 Wallis, S.S., Ventimiglia, L.N., Otigbah, E., Infante, E., Cuesta-Geijo, M.A., Kidiyoor, G.R., Carbajal, M.A.,
1018 Fleck, R.A., Foiani, M., Garcia-Manyes, S., et al. (2021). The ESCRT machinery counteracts Nesprin-2G-
1019 mediated mechanical forces during nuclear envelope repair. Dev Cell *56*, 3192-3202 e3198.
1020 10.1016/j.devcel.2021.10.022.

1021 Webster, B.M., Colombi, P., Jäger, J., and Lusk, C.P. (2014). Surveillance of nuclear pore complex
1022 assembly by ESCRT-III/Vps4. Cell *159*, 388-401. 10.1016/j.cell.2014.09.012.

1023 Webster, B.M., Thaller, D.J., Jäger, J., Ochmann, S.E., Borah, S., and Lusk, C.P. (2016). Chm7 and Heh1
1024 collaborate to link nuclear pore complex quality control with nuclear envelope sealing. EMBO J *35*, 2447-
1025 2467. 10.15252/embj.201694574.

1026 West, R.R., Vaisberg, E.V., Ding, R., Nurse, P., and McIntosh, J.R. (1998). cut11(+): A gene required for
1027 cell cycle-dependent spindle pole body anchoring in the nuclear envelope and bipolar spindle formation in
1028 *Schizosaccharomyces pombe*. Mol Biol Cell *9*, 2839-2855. 10.1091/mbc.9.10.2839.

1029 Wood, V., Gwilliam, R., Rajandream, M.A., Lyne, M., Lyne, R., Stewart, A., Sgouros, J., Peat, N., Hayles,
1030 J., Baker, S., et al. (2002). The genome sequence of *Schizosaccharomyces pombe*. Nature *415*, 871-880.
1031 10.1038/nature724.

1032 Woodruff, J.B., Ferreira Gomes, B., Widlund, P.O., Mahamid, J., Honigmann, A., and Hyman, A.A. (2017).
1033 The centrosome Is a selective condensate that nucleates microtubules by concentrating tubulin. Cell *169*,
1034 1066-1077 e1010. 10.1016/j.cell.2017.05.028.

1035 Zhang, X.R., Zhao, L., Suo, F., Gao, Y., Wu, Q., Qi, X., and Du, L.L. (2022). An improved auxin-inducible
1036 degron system for fission yeast. G3 (Bethesda) *12*, jkab393. 10.1093/g3journal/jkab393.

1037 Zwicker, D., Decker, M., Jaensch, S., Hyman, A.A., and Julicher, F. (2014). Centrosomes are autocatalytic
1038 droplets of pericentriolar material organized by centrioles. Proc Natl Acad Sci U S A *111*, E2636-2645.
1039 10.1073/pnas.1404855111.
1040

Supplementary Table S1. GFP-tagging of key ESCRT machinery			
Protein	Orthologs		GFP tagging approach
S. pombe	*S. cerevisiae*	*H. sapiens*	
Cmp7	Chm7	CHMP7	Endogenous, C-terminal 3×HA-mEGFP
Vps32	Snf7	CHMP4A-C	Ectopic in *vps32*Δ, N-terminal 3×HA-mEGFP
Ist1	Ist1	IST1	Endogenous, C-terminal 3×HA-mEGFP
Vps24	Vps24	CHMP3	Ectopic in *vps24*Δ, N-terminal 3×HA-mEGFP
Did4	Vps2	CHMP2A,B	Ectopic in did*4*Δ, N-terminal 3×HA-mEGFP
Did2	Did2	CHMP1A,B	Endogenous, C-terminal 3×HA-mEGFP

Supplementary Table S2. Complete list of *S. pombe* strains used in this study		
Strain (MKSP)	**Genotype**	**Origin**
280	*pcp1::pcp1-15-HA::hygMX6* | *leu1-32* | *ura4-D18* | *h-*	CSF0076 (Fong et al., 2010); gift from Takashi Toda
281	*pcp1::pcp1-18-HA::hygMX6* | *leu1-32* | *ura4-D18* | *h-*	CSF0082 (Fong et al., 2010); gift from Takashi Toda
399	*leu1-32* | *ura4-D18* | *h+*	Lab stock
1474	*natMX6::nmt81-GFP-Kms2-3'::kanMX6 (kms2 DAmP)* | *aurR-pnda3-mCherry-atb2*| *ade6-M?* | *ura4-D18* | *leu1-32* | *h-*	Constructed in Wälde et al., 2014
1697	*cut11::cut11-GFP:ura4+* | *aurR-pnda3-mCherry-atb2* | *ade6-M?* | *leu1?* | *ura4-D18* | *h-*	Constructed in this work, derived from CSF0511 (Fong et al., 2010) and PN#3779 (West et al., 1998)
3180	*cdc7::cdc7-GFP:kanMX6* | *pcp1::pcp1-mCherry:kanMX6* | *leu1-32* | *ura4-D18*	This work
3186	*fta3::fta3-mEGFP::kanMX6* | *leu1-32* | *ura4-D18* | *ade6-M210*	MSA007 (Pollard Lab)
3243	*cmp7::hygMX6* | *cdc7::cdc7-GFP:kanMX6* | *pcp1::pcp1-mCherry:kanMX6* | *leu1-32* | *ura4-D18*	This work
3248	*heh1::natMX6* | *leu1-32* | *ura4-D18* | *ade6-M21?* | *h+*	This work
3259	*cmp7::cmp7-3×HA-mEGFP:kanMX6* | *heh1::natMX6* | *aurR-pnda3-mCherry-atb2* | *leu1-32* | *ura4-D18*	Constructed in this work, derived from CSF0511 (Fong et al., 2010)
3275	*cmp7::cmp7-3×HA-mEGFP:kanMX6* | *heh2::hygMX6* | *aurR-pnda3-mCherry-atb2* | *leu1-32?* | *ura4-D18?*	Constructed in this work, derived from CSF0511 (Fong et al., 2010)
3334	*leu1::*P_{did4}*-mEGFP-3×HA-did4-*T_{did4} | *did4::hygMX6* | *sad1::sad1-mCherry:kanMX6* | *aurR-pnda-mCherry-atb2* | *ura4-D18* | *h-*	Constructed in this work, derived from CSF0511 (Fong et al., 2010)
3340	*cmp7::natMX6* | *aurR-pnda3-mCherry-atb2* | *leu1-32* | *h+*	Constructed in this work, derived from CSF0511 (Fong et al., 2010)
3342	*did2::did2-3×HA-mEGFP:kanMX6* | *pcp1::pcp1-mCherry:natMX6* | *aurR-pnda3-mCherry-atb2* | *leu1-32* | *ura4-D18* | *h-*	Constructed in this work, derived from CSF0511 (Fong et al., 2010)
3345	*leu1::P41nmt1-MBP-yeGFP-4×MBP-*T_{cyc1} | ura4-D18 | h+	This work
3352	*leu1::*P_{vps24}*-mEGFP-3×HA-vps24-*T_{vps24} | *vps24::hygMX6* | *pcp1::pcp1-mCherry:kanMX6* | *aurR-pnda-mCherry-atb2* | *ura4-D18* | *h-*	Constructed in this work, derived from CSF0511 (Fong et al., 2010)
3353	*leu1::*P_{vps32}*-mEGFP-3×HA-vps32-*T_{vps32} | *vps32::hygMX6* | *pcp1::pcp1-mCherry:natMX6* | *aurR-pnda-mCherry-atb2* | *ura4-D18* | *h-*	Constructed in this work, derived from CSF0511 (Fong et al., 2010)
3354	*leu1::*P_{vps32}*-mEGFP-3×HA-vps32-*T_{vps32} | *vps32::hygMX6* | *cmp7::natMX6* | *pcp1::pcp1-mCherry:kanMX6* | *aurR-pnda-mCherry-atb2* | *ura4-D18* | *h?*	Constructed in this work, derived from CSF0511 (Fong et al., 2010)
3355	*leu1::*P_{vps24}*-mEGFP-3×HA-vps24-*T_{vps24} | *vps24::hygMX6* | *cmp7::natMX6* | *pcp1::pcp1-mCherry:kanMX6* | *aurR-pnda-mCherry-atb2* | *ura4-D18*	Constructed in this work, derived from CSF0511 (Fong et al., 2010)
3363	*cmp7::cmp7-3×HA-mEGFP:kanMX6* | *pcp1::pcp1-mCherry:natMX6* | *aurR-pnda3-mCherry-atb2* | *leu1-32* | *ura4-D18* | *h-*	Constructed in this work, derived from CSF0511 (Fong et al., 2010)
3365	*ist1::ist1-3×HA-mEGFP:kanMX6* | *sad1::sad1-mCherry:natMX6* | *aurR-pnda3-mCherry-atb2* | *leu1-32* | *ura4-D18* | *h-*	Constructed in this work, derived from CSF0511 (Fong et al., 2010)
3366	*leu1::*P_{did4}*-mEGFP-3×HA-did4-*T_{did4} | *did4::hygMX6* | *cmp7::natMX6* | *sad1::sad1-mCherry:kanMX6* | *aurR-pnda-mCherry-atb2* | *ura4-D18*	Constructed in this work, derived from CSF0511 (Fong et al., 2010)

Supplementary Table S2. Complete list of *S. pombe* strains used in this study		
Strain (MKSP)	**Genotype**	**Origin**
3381	*cmp7::cmp7-3×HA-mEGFP:kanMX6 | did4::hygMX6 | pcp1::pcp1-mCherry:natMX6 | aurR-pnda3-mCherry-atb2 | leu1-32 | ura4-D18*	Constructed in this work, derived from CSF0511 (Fong et al., 2010)
3385	*cmp7::cmp7-3×HA-mEGFP:kanMX6 | vps32::hygMX6 | aurR-pnda3-mCherry-atb2 | leu1-32 | ura4-D18*	Constructed in this work, derived from CSF0511 (Fong et al., 2010)
3387	*cmp7::cmp7-3×HA-mEGFP:kanMX6 | vps24::hygMX6 | aurR-pnda3-mCherry-atb2 | leu1-32 | ura4-D18*	Constructed in this work, derived from CSF0511 (Fong et al., 2010)
3420	*cmp7::natMX6 | pcp1::pcp1-15-HA::hygMX6 | leu1-32 | ura4-D18 | h+*	Constructed in this work, derived from CSF0511 (Fong et al., 2010)
3425	*cmp7::kanMX6 | pcp1::pcp1-18-HA::hygMX6 | leu1-32 | ura4-D18 | h+*	Constructed in this work, derived from CSF0511 (Fong et al., 2010)
3429	*cmp7::cmp7-3×HA-mEGFP:kanMX6 | ist1::hygMX6 | pcp1::pcp1-mCherry:natMX6 | aurR-pnda3-mCherry-atb2 | leu1-32 | ura4-D18*	Constructed in this work, derived from CSF0511 (Fong et al., 2010)
3447	*ist1::ist1-3×HA-mEGFP:kanMX6 |cmp7::hygMX6 | sad1::sad1-mCherry:natMX6 | aurR-pnda3-mCherry-atb2 | leu1-32 | ura4-D18 | h?*	Constructed in this work, derived from CSF0511 (Fong et al., 2010)
3449	*leu1::P_{vps32}-mEGFP-3×HA-vps32-T_{vps32} | vps32::hygMX6 | ist1::kanMX6 | pcp1::pcp1-mCherry:natMX6 | aurR-pnda-mCherry-atb2 | ura4-D18*	Constructed in this work, derived from CSF0511 (Fong et al., 2010)
3488	*leu1::P41$_{nmt1}$-MBP-yeGFP-4×MBP-T_{cyc1} | aurR-pnda-mCherry-atb2 | ura4-D18 | h+*	This work
3496	*ist1::ist1-3×HA-mEGFP:kanMX6 |did4::hygMX6 | sad1::sad1-mCherry:natMX6 | aurR-pnda3-mCherry-atb2 | leu1-32 | ura4-D18*	Constructed in this work, derived from CSF0511 (Fong et al., 2010)
3501	*leu1::P41$_{nmt1}$-MBP-yeGFP-2×MBP-T_{cyc1} | cmp7::hygMX6 | aurR-pnda-mCherry-atb2 | ura4-D18 | h+*	This work
3504	*ist1::ist1-3×HA-mEGFP:kanMX6 | vps32::hygMX6 | sad1::sad1-mCherry:natMX6 | aurR-pnda3-mCherry-atb2 | leu1-32 | ura4-D18*	Constructed in this work, derived from CSF0511 (Fong et al., 2010)
3511	*leu1::P_{vps24}-mEGFP-3×HA-vps24-T_{vps24} | vps24::hygMX6 | did4:kanMX6 | pcp1::pcp1-mCherry:kanMX6 | aurR-pnda-mCherry-atb2 | ura4-D18 | h-*	Constructed in this work, derived from CSF0511 (Fong et al., 2010)
3517	*cmp7::cmp7-XTEN16-3×sAID:kanMX6 | ura4::Padh1-OsTIR1-F74A | leu1-32 | ade6?*	Constructed in this work, derived from DY48569 (Zhang et al., 2022)
3521	*cmp7::cmp7-3×HA-mEGFP:kanMX6 | ist1::ist1-3×HA-mCherry:kanMX6 | leu1-32 | ura4-D18 | h-*	This work
3535	*leu1::P41$_{nmt1}$-MBP-yeGFP-4×MBP | cmp7::hygMX6 | aurR-pnda-mCherry-atb2 | ura4-D18 | ade6-M210 | h-*	This work
3544	*ist1::ist1-3×HA-mEGFP:kanMX6 | vps24::kanMX6 | sad1::sad1-mCherry:natMX6 | aurR-pnda3-mCherry-atb2 | leu1-32 | ura4-D18*	Constructed in this work, derived from CSF0511 (Fong et al., 2010)
3557	*leu1::P41$_{nmt1}$-MBP-yeGFP-4×MBP-T_{cyc1} | vps32::hygMX6 | aurR-pnda-mCherry-atb2 | ura4-D18 | h+*	This work
3559	*leu1::P41$_{nmt1}$-MBP-yeGFP-4×MBP-T_{cyc1} | ist1::kanMX6 | aurR-pnda-mCherry-atb2 | ura4-D18 | h+*	This work
3586	*leu1::P41$_{nmt1}$-MBP-yeGFP-4×MBP-T_{cyc1} | did4::hygMX6 | aurR-pnda-mCherry-atb2 | ura4-D18 | h+*	This work
3592	*leu1::P41$_{nmt1}$-MBP-yeGFP-4×MBP-T_{cyc1} | vps24::kanMX6 | aurR-pnda-mCherry-atb2 | ura4-D18 | h+*	This work
3593	*leu1::P41$_{nmt1}$-MBP-yeGFP-4×MBP-T_{cyc1} | did2::hygMX6 | aurR-pnda-mCherry-atb2 | ura4-D18 | h+*	This work

Supplementary Table S2. Complete list of *S. pombe* strains used in this study		
Strain (MKSP)	**Genotype**	**Origin**
3625	*ist1::ist1-3×HA-mEGFP:kanMX6 | cmp7-XTEN16-3×sAID::kanMX6 | ura4+::P_{adh1}-OsTIR1$_{F74A}$ | sad1::sad1-mCherry:natMX6 | aurR-pnda3-mCherry-atb2 | leu1-32 | ade6-M216*	Constructed in this work, derived from CSF0511 (Fong et al., 2010) and DY48569 (Zhang et al., 2022)
3635	*leu1::P41$_{nmt1}$-MBP-yeGFP-4×MBP | heh1::kanMX6 | aurR-pnda-mCherry-atb2 | ura4-D18 | h-*	This work
3668	*leu1::P_{did4}-mEGFP-3×HA-did4-T_{did4} | did4::hygMX6 | ist1::natMX6 | sad1::sad1-mCherry:kanMX6 | aurR-pnda-mCherry-atb2 | ura4-D18*	Constructed in this work, derived from CSF0511 (Fong et al., 2010)
3669	*leu1::P_{vps24}-mEGFP-3×HA-vps24-T_{vps24} | vps24::hygMX6 | ist1::natMX6 | pcp1::pcp1-mCherry:natMX6 | aurR-pnda-mCherry-atb2 | ura4-D18*	Constructed in this work, derived from CSF0511 (Fong et al., 2010)
3683	*cmp7::hygMX6 | natMX6::nmt81-GFP-Kms2-3'::kanMX6 (kms2 DAmP) | aurR-pnda3-mCherry-atb2| ade6-M? | ura4-D18 | leu1-32 | h-*	This work
3699	*leu1::P41$_{nmt1}$-MBP-yeGFP-4×MBP-T_{cyc1} | cmp7::cmp7-XTEN16-3×sAID:kanMX6 | ura4::P_{adh1}-OsTIR1$_{F74A}$ | cut11::cut11-mCherry:natMX6 | h+*	Constructed in this work, derived from DY48569 (Zhang et al., 2022)
3811	*leu1::P41$_{nmt1}$-MBP-yeGFP-4×MBP-T_{cyc1} | cmp7::natMX6 | pcp1::pcp1-15-HA::hygMX6 | cut11::cut11-mCherry:natMX6 | ura4-D18 | h+*	Constructed in this work, derived from CSF0511 (Fong et al., 2010)
3812	*leu1::P41$_{nmt1}$-MBP-yeGFP-4×MBP-T_{cyc1} | pcp1::pcp1-15-HA::hygMX6 | cut11::cut11-mCherry:natMX6 | ura4-D18 | h+*	Constructed in this work, derived from CSF0511 (Fong et al., 2010)
3838	*heh1::natMX6 | pcp1::pcp1-15-HA::hygMX6 | leu1-32 | ura4-D18 | h?*	Constructed in this work, derived from CSF0511 (Fong et al., 2010)
3839	*heh1::natMX6 | pcp1::pcp1-18-HA::hygMX6 | leu1-32 | ura4-D18 | h?*	Constructed in this work, derived from CSF0511 (Fong et al., 2010)
3843	*heh1::hygMX6 | natMX6::nmt81-GFP-Kms2-3'::kanMX6(kms2 DAmP) | aurR-pnda3-mCherry-atb2| ade6-M? | ura4-D18 | leu1-32 | h?*	This work

Supplementary Table S3. Complete list of plasmids used in this study			
Identifier	**Name/Description**	**Usage**	**Origin**
pNA8	pFA6a-3×HA-mEGFP-KanMX6	Template for PCR based chromosomal integration of 3×HA-mEGFP ORF	This study; Addgene 87023
pNA22	pJK148-P_{vps32}-mEGFP-3×HA-vps32-T_{vps32}	Linearized with NruI and transformed into MKSP975	This study, Gibson assembly
pNA23	pJK148-P_{vps24}-mEGFP-3×HA-vps24-T_{vps24}	Linearized with NruI and transformed into MKSP975	This study, Gibson assembly
pNA33	pFA6a-hygMX6	Integration cassette amplification hygMX6 template	Hentges et al., 2005
pNA34	pFA6a-natMX6	Integration cassette amplification natMX6 template	Hentges et al., 2005
pNA35	pFA6a-kanMX6	Template for PCR based chromosomal integration of kanMX6 ORF	Wach et al., 1997; Addgene 39296
pNA45	pJK148-P_{did4}-mEGFP-3×HA-did4-T_{did4}	Linearized with NruI and transformed into MKSP975	This study, Gibson assembly
pNA47	pFA6a-mCherry-KanMX6	Template for PCR based chromosomal integration of mCherry ORF	EUROSCARF
pNA48	pFA6a-mCherry-NatMX6	Template for PCR based chromosomal integration of mCherry ORF	EUROSCARF
pNA50	pFA6a-3×HA-mCherry-NatMX6	Template for PCR based chromosomal integration of 3×HA-mCherry ORF	This study
pNA63	pJK148-$P41_{nmt1}$-MBP-yeGFP-4×MBP-T_{cyc1}	Linearized with NruI and transformed into MKSP399	Popken et al., 2015 and this study, restriction digest cloning
pDB4581	pFA6a-3×sAID-KanMX6	Template for PCR based chromosomal integration of 3×sAID ORF	Zhang et al., 2022; Addgene 171124